doi:10.1038/nature17176

Recent near-Earth supernovae probed by global deposition of interstellar radioactive ^{60}Fe

A. Wallner[1], J. Feige[2], N. Kinoshita[3], M. Paul[4], L.K. Fifield[1], R. Golser[2], M. Honda[5], U. Linnemann[6], H. Matsuzaki[7], S. Merchel[8], G. Rugel[8], S.G. Tims[1], P. Steier[2], T. Yamagata[9], S.R. Winkler[2]

List of sections, tables and figures in the supplementary information:

Supplementary Tables:

- **Supplementary Table S1:** Summary of the three different archives.
- **Supplementary Table S2:** Summary of AMS machine parameters of the four AMS facilities used in this work.
- **Supplementary Table S3**: $^{60}Fe/Fe$ isotope ratios from AMS measurement on 52 sediment samples (Eltanin) from the Indian Ocean.
- **Supplementary Table S4**: $^{60}Fe/Fe$ measurement data for the individual sediment samples.
- **Supplementary Table S5**: $^{60}Fe/Fe$ measurement data for the individual Crust-2 samples (not background- or decay corrected data).
- **Supplementary Table S6**: Deposition rates and ^{60}Fe concentrations for averaged sediment data with time resolution of ~100-250 kyr.
- **Supplementary Table S7**: Sedimentation rates (sediments E49-53 and E45-21) and growth rates (crust, nodules).
- **Supplementary Table S8:** properties of various massive stars – ^{60}Fe yields and comparison with the measured ^{60}Fe influx assumed to be equally distributed within a volume of 50 pc.

Supplementary Figures:

- **Supplementary Figure S1:** Locations for new and previous deep-sea ^{60}Fe archives.
- **Supplementary Figure S2:** Separation of ^{60}Fe from the isobar ^{60}Ni.
- **Supplementary Figure S3**: ^{60}Fe/Fe isotope ratios for sediment samples and commercial iron (Fe_2O_3) blank material.
- **Supplementary Figure S4:** Measured ^{60}Fe/Fe isotope ratios for the two FeMn nodule samples.
- **Supplementary Figure S5:** 150 kyr-averages of ^{60}Fe concentrations and depositions rates for the Eltanin sediment.
- **Supplementary Figure S6:** Comparison of the measured ^{60}Fe deposition rates from the sediment data (black squares) with models of interplanetary influx of ^{60}Fe.
- **Supplementary Figure S7:** ^{60}Fe survival fraction versus distance for three different ^{60}Fe SN-nucleosynthesis yields.
- **Supplementary Figure S8:** ^{60}Fe nucleosynthesis yields.
- **Supplementary Figure S9**: measured (not decay-corrected isotope ratios) ^{60}Fe/Fe for the sediment samples (1σ uncertainties).
- **Supplementary Figure S10**: Measured (not decay-corrected) isotope ratios ^{26}Al/^{27}Al and ^{10}Be/^{9}Be isotope ratios of E45-21 and E49-53 versus age.
- **Supplementary Figure S11**: Measured ^{10}Be/^{9}Be (top) and ^{26}Al/^{27}Al (bottom) isotope ratios for the two ELTANIN sediment cores E-49-53 and E45-21
- **Supplementary Figure S12**: measured (not decay-corrected) ^{10}Be/^{9}Be isotope ratios for the two crust samples versus depth.
- **Supplementary Figure S13**: measured (not decay-corrected) ^{10}Be/^{9}Be isotope ratios for the two nodule samples versus depth.

Measured radionuclides in the archives and dating (all data are 1σ, unless noted)

Three different time-resolved deep-sea archives were selected for the present study of extra-terrestrial ^{60}Fe (Supplementary Figure S1, note the crust and sediment samples are different to those used by Knie *et al.*[10,11] and Fitoussi et al.[18]). In total 139 individual samples from these three different archives were measured for their ^{10}Be ($t_{1/2}$=1.387 Myr)[31-36], ^{26}Al (0.71 Myr) or ^{60}Fe signatures (Supplementary Table S1). Each archive is described in detail below.

Typically 3g sediment and 200-700 mg nodule was used to leach and separate simultaneously Al, Be and Fe[37] i.e. to extract preferentially the authigenic fraction of the sample. ~100–500 mg of crust material was dissolved to isolate Fe and Be. We have applied the most sensitive technique, accelerator mass spectrometry (AMS)[38-40] to detect the minute amounts of ^{60}Fe (ANU)[8,41], ^{10}Be (VERA[42] MALT[43], HZDR[44]) and ^{26}Al (VERA)[45] via their isotope ratios ^{60}Fe/Fe, ^{26}Al/^{27}Al and ^{10}Be/^{9}Be (Supplementary Table S2). The respective concentrations of the radionuclides ^{60}Fe, ^{26}Al and ^{10}Be were derived from the concentrations of the stable Fe, Al and Be determined via ICP-MS and AAS (see below).

Dating of the various archives employed ^{10}Be and ^{26}Al. Both radioisotopes are produced by cosmic-ray induced spallation of nitrogen and oxygen, and argon, respectively, in the Earth atmosphere at roughly constant rates, if averaged over time periods of ~kyr, and are incorporated into marine archives. Their subsequent radioactive decay therefore serves as a clock and for ^{10}Be this has been widely used to provide chronologies for marine sediments and FeMn crusts[33,34]. Although ^{26}Al is produced and ejected by SN explosions, a potential SN signal of ^{26}Al is likely to be small compared to its terrestrial production and would sit on top of this background (see below). Thus, ^{26}Al was measured for all available sediment samples and complemented the ^{60}Fe data[21,36]. In contrast to ^{60}Fe, however, we did not detect any significant deviations from a constant (decay-corrected) terrestrial background (see below).

For the Eltanin sediment samples, the pre-existing paleomagnetic dating[35] was refined using both, $^{10}Be/^{9}Be$ and $^{26}Al/^{27}Al$ isotope ratios as these data were matched to the known reversals of the Earth's magnetic field[21,36]. The absolute ages for the sediment samples are uncertain by 0.1 Myr for ages up to 3.2 Myr. For the two older sediment samples (E45-16) we deduced ages between 4 and ~7 Myr. At ages greater than 4 Myr, radiogenic production of ^{26}Al within the sediment might become important, leading to deviations from ages obtained from ^{10}Be dating[21,54]. For Crust-1 we deduce from our ^{10}Be data an uncertainty in the absolute ages of 0.3 Myr. A few mm of the top layer of Crust-2 had been removed when we obtained the sample, thus its absolute depth was normalized by assuming the same $^{10}Be/^{9}Be$ ratio for the surface layer as measured for Crust-1. Consequently, we infer an uncertainty in the absolute ages of Crust-2 of 0.5 Myr. Due to changes in the growth rates by a factor of 2 over ~5 Myr, we assume the same uncertainty of 0.5 Myr for the nodules.

^{60}Fe measurement signal

Four sediment cores (52 individual samples, each ~1cm thick) from the Indian Ocean[35] provided a record with a time resolution of <30 kyr that extended from the recent past to ~5-7 Myr BP. The interstellar ^{60}Fe is released and dissolved from the interplanetary dust particles when they arrive at the surface of the ocean and is then transferred to the sediments via scavenging processes into the sedimentary archives. The measured $^{60}Fe/Fe$ atom-ratios averaged over 300 kyr are listed in Table 1 (individual data are listed in Supplementary Table S4). Overall, 291 ^{60}Fe events were registered, of which 288 (45 samples) were from the time period 1.71-3.18 Myr. The recent period (<0.2 Myr) is represented by five sediment samples from two different cores. Their $^{60}Fe/Fe$ ratio is compatible with the measurement background (Supplementary Figures S2 and S3) as is the ratio of two samples at ages older than 4-5 Myr;

i.e. none of the recent (<0.2 Myr) and old (≥5 Myr) samples show any evidence for ^{60}Fe above background.

The two Pacific crust samples cover a longer time period, due to a growth rate ~10^3 times less than sediments: Crust-1, subdivided into five 0.5 cm thick sublayers, provides ^{60}Fe data from present to 10.9 Myr, averaged over ~2.2 Myr. The first two layers gave ^{60}Fe signals 4σ and 7σ above background. Layers 3 and 5 have ratios ($^{60}Fe/Fe=(0.14\pm0.08)\times10^{-15}$) that are close to the background, but layer 4, which spans the period 6.5-8.7 Myr, has a significantly higher ratio (~4σ above background, Table 2).

Crust-2, subdivided into 26 thin layers (0.5–1 mm), spans a continuous time period from 1.2–7 Myr BP with ~0.15–0.3 Myr per layer and an uncertainty in the absolute age of 0.3 Myr. The $^{60}Fe/Fe$ data, averaged over two to three layers to give a ~0.3–0.5 Myr time-resolution, are listed in Table 2. Again, a clear ^{60}Fe-signal is observed. Beyond 3.1 Myr BP the $^{60}Fe/Fe$ ratio drops drastically and becomes indistinguishable from background at ~3.5 Myr. All 14 layers beyond 3.5 Myr are compatible with the measurement blanks ($^{60}Fe/Fe<0.03\times10^{-15}$).

Two nodule samples (Atlantic), each with ~0.4-3 Myr time-resolution per layer, covered 5.4 Myr BP. Elevated $^{60}Fe/Fe$ values were measured for the second layer of nodule-21 (1.8-3.3 Myr), and the first two layers (0-3.4 Myr) of nodule-24. Although statistical precision is lower due to low absolute $^{60}Fe/Fe$ ratios, the nodules support the trend of ^{60}Fe in the other archives, suggesting a maximum at ~1–3 Myr and no significant ^{60}Fe in the period 3.3–5.4 Myr (Table 3).

Deposition rates of ^{60}Fe into archives

Deposition rates (atoms·cm^{-2}·yr^{-1}) were calculated from the decay-corrected ^{60}Fe/Fe-ratios, the leachable stable Fe content, the mean density of the archives and their sedimentation or growth rates. Integration over the respective time periods gives the ^{60}Fe deposition (sediments) or incorporation (crusts, nodules) into the archives. Calculation of the extraterrestrial ^{60}Fe flux and fluence (time-integrated flux) was based on the sediment and crust data (which was corrected for incorporation efficiency as determined from the sediment yields) and the Earth's cross section.

Based on the relative amounts of ^{60}Fe in layers 1 and 2 of Crust-1, we estimate that <15% of the ^{60}Fe in the sediment is missed outside of the range of the data. Deep-sea sediments are expected to incorporate all ^{60}Fe from the water column above due to the high particle reactivity which results in 100% transfer into the sediments. By comparison, the ^{60}Fe incorporation-efficiency into Crust-1 and Crust-2 is deduced to be (17±3)% and ~7%, respectively, assuming that the ^{60}Fe-signal is distributed uniformly over Earth's surface. For Crust-1, this value is consistent with that of Pu into similar material (21±5%)[6]. The nodules have even lower efficiencies (2–4%).

Our data imply that incorporation efficiencies into deep-sea crust is a factor of 10–30 higher than the value of 0.6% estimated in Knie *et al.*[11] (see also Ref. 46). The incorporation of (1.5±0.4)×10^{6} atoms·cm^{-2} measured by [11] over essentially the same time interval (1.7–2.6 Myr, adjusted for revised ^{10}Be and ^{60}Fe half-lives)[18,36] is similar to both crusts measured in the present work; thus our data suggest a ~10 times lower interstellar fluence than estimated in [11].

Expected ^{60}Fe influx from meteorites or micrometeorites

The high-resolution data in the younger signal over a period of ~1.5 Myr (sediment, Crust-2) is expected to reflect the time-dependent ^{60}Fe-flux into the SS (150kyr-averages of deposition rates into and ^{60}Fe concentrations in the sediment are plotted in Supplementary Figure S5), since the residence time of Fe in the ocean is negligible and any ^{60}Fe in dust grains that were ablated in the atmosphere are eventually incorporated into sediments (~10–20% into crusts). We assume that extraterrestrial ^{60}Fe is homogenously distributed over Earth's surface (5.1×10^{18} cm^2), and derive from our data that $1.8(1.0)\times10^{26}$ ^{60}Fe atoms reached Earth (~18 and 11 kg) during the two time periods with elevated ^{60}Fe (1.5–3.2 Myr and 6.5–8.7 Myr).

Each year ~(30,000±20,000) tonnes of cosmic dust reaches Earth[47], predominantly through micrometeorites (MM) and interplanetary dust-particles (IDP's). Meteorites contribute less than 1% of the total mass flux. Typical concentrations of ^{60}Fe in micrometeorites or interplanetary dust are 0.51 dpm (decays per minute)$\cdot kg^{-1}$ Ni (1×10^{12} ^{60}Fe atoms$\cdot kg^{-1}$ Ni)[48,49]. As the Ni content in cosmic dust (interplanetary particles) is ~1% (CI chondrites) we calculate a flux of 3×10^{17} ^{60}Fe atoms$\cdot yr^{-1}$. Evenly spread over Earth's surface, this corresponds to 0.06 ^{60}Fe atoms$\cdot cm^{-2}$ yr^{-1} (see Supplementary Figure S6). In contrast, we measured a mean ^{60}Fe flux of 24 (21) ^{60}Fe atoms$\cdot cm^{-2}$ yr^{-1} between 1.7 and 3.2 Myr (6.5–8.7 Myr, Table 1), i.e. the observed ^{60}Fe influx is ~400 times higher than expected from a constant influx of interplanetary particles. Thus the ^{60}Fe-influx between 1.5–3.2 and 6.5–8.7 Myr would require a two to three orders of magnitude enhancement in MM and IDP influx over these two ~2 Myr periods. Data obtained over 80 Myr in Pacific deep-sea sediment cores do not indicate any systematic deviation in the mean flux over the last 80 Myr (except the K/T boundary)[50] and agree with the Long-Duration-Exposure-Facility (LDEF) satellite study of cosmic dust[45]. Recent other work indicates even lower dust influx[51-53].

Noting that the coincidently named 'Eltanin' impact of an asteroid with ~2 km diameter occurred in the SE Pacific Ocean ~2.5 Myr ago, production of ^{60}Fe in Ni of a massive asteroid body is another possibility that must be considered: The generation of 1.8×10^{26} ^{60}Fe atoms would, however, require that 1.8×10^{14} kg of Ni in meteorite material be exposed to cosmic rays in space for a time long compared to the ^{60}Fe half-life of 2.6 Myr. Penetration depths of cosmic rays are a few meters. Even for a 10 km diameter (~ the size of the body assumed responsible for the K/T event, 65 Myr ago) and assuming a penetration depth of 3m, only 4×10^{10} kg of Ni would have been exposed to cosmic rays. This is ~4500 times less than would be required to account for the observed ^{60}Fe excess. We conclude that the ^{60}Fe signal cannot originate from break-up of a single large scale object.

Furthermore, we also measured the Ni content in the various archives. For Crust-1 Ni contents were [Ni]~0.35% atom/atom, compared to [Fe]~10–13% (similar for Crust-2 and the nodules). The sediments contained on average 40µg leachable Ni per g sediment, compared to 0.17% of leached Fe (Table 1). Thus, the different archives all give [Ni]/[Fe] concentrations between 0.02 and 0.03 atom/atom (see also ref. 18). With 1×10^{12} ^{60}Fe atoms per kg Ni, we calculate for the sediment samples a $^{60}Fe/Fe$-ratio of 2.4×10^{-15}, ~50% lower than the average measured between 1.7 and 3.2 Myr. Thus, even for the most extreme and unlikely case that all Ni in the archives would be of micro(meteoritic) origin, i.e. all archives do not contain any terrestrial Ni, we cannot account for the measured ^{60}Fe. The Ni content was found to vary by less than 50% from the average value in the crust and by less than 10% in the sediment, and it is not different for layers outside the ^{60}Fe-signal. Thus, we would expect the same decay-corrected ^{60}Fe-content for all layers if its origin is cosmic-ray spallation on Ni. Note, as the signal was found globally, the required global cosmic dust flux (containing 1% Ni) would become 7×10^{6} tonnes using the sediment (crust) Ni-data, this is ≥230 times higher than the measured cosmic dust flux[47]. In turn, if –similar to Ni– the leached stable Fe would also be of extraterrestrial origin, the required cosmic dust flux would become another factor of ~40, i.e. 4 orders of magnitudes higher than measured.

^{26}Al-data and ^{60}Fe/^{26}Al ratios

Because terrestrial production of ^{26}Al is substantially higher than the expected influx from extraterrestrial sources, an extraterrestrial ^{26}Al-signal distributed over ~2 Myr will be hidden within the large terrestrial signal. Indeed, no significant ^{26}Al signal above the terrestrial signal was observed in our data[36,21,54] (Supplementary Figure S10, publication in preparation). Assuming that any extraterrestrial signal would have the same time distribution as ^{60}Fe, a limit of >0.5 on the ^{60}Fe/^{26}Al atom ratio in extraterrestrial material is deduced. This atom-ratio corresponds to a ratio in their decay rates of >0.15 and can be compared to the measured ^{60}Fe/^{26}Al γ-flux ratio of (0.15±0.05)[2,9].

^{60}Fe survival fraction in dust

The measured ^{60}Fe deposition can be linked to the ^{60}Fe ISM-fluence and nucleosynthesis yields through the ^{60}Fe survival-fraction, f_{60}. This is the product of the probabilities that ^{60}Fe ejected by the star is captured in dust grains, that it survives in the ISM and penetrates the SS. Interstellar dust particles were detected at Earth orbit[15,55,56]. Recent observations suggest that the major fraction of refractory elements like Fe will be condensed into dust particles shortly after a SN-explosion[57]. Dust grains have to be >0.2μm in size to survive from the SN into the ISM essentially unchanged[57,58]. Infrared observations of recent SNe suggest that a large fraction of grains is larger than this size within years of the explosion[57] and could thus potentially survive the disruptive effect of the reverse shock as it expands through the ejecta as well as destruction processes in the ISM.

For SN-ejecta penetrating the SS, f_{60} is calculated by assuming ^{60}Fe equally distributed over a surface area of the respective distance and then compared with the measured ^{60}Fe-fluence into the inner SS. Distances of such events are constraint as follows: <20pc is excluded, otherwise the intense cosmic-ray flux would have triggered global climatic and biological impacts[16,17,56,59,60]. We use an upper limit of 100pc, i.e. within the limits of the LB. SN dust-particles have velocities of 30-150 km/s which are higher than those of normal ISM dust-particles[3]. Their SN survival-size is already comparable to the satellite data, thus there would not be large filtering and deflection of SN dust-particles by the SS at all. Hence, the ^{60}Fe-flux at Earth's orbit may be roughly unaltered from the ISM. We deduce the factor f_{60} largely represents the survival fraction of ^{60}Fe in the first violent phase when ejected from the SN.

If we assume a total ^{60}Fe-yield of 9×10^{-5} $M_{\odot}$[24-28,61], (e.g. assume a superposition of 3 SNe each with 3×10^{-5} $M_{\odot}$[24-28,61] (Supplementary Figure S8) was responsible for the observed ^{60}Fe time-profile in the 1.5-Myr interval at 1.7–3.2 Myr), we calculate with our measured ^{60}Fe deposition of $(3.5\pm0.2)\times10^{7}$ atoms·cm^{-2} a number for f_{60} between 0.4 and 9% (depending on distance, and uncertain by a factor of three from the SN-nucleosynthesis yields, Supplementary Figure S7). Consequently, a lower survival-fraction would imply closer SN-event(s), which could have had a severe impact on Earth's climate and possibly the more advanced life forms.

Comparison with the interstellar influx of ^{244}Pu and the observed ^{60}Fe decay in the ISM

The measured deposition-rate for ^{60}Fe can be compared directly to recent experimental data for the *r*-process nuclide ^{244}Pu into the same archives[6,62,63]. This comparison is largely independent of factors such as SS-penetration, dust survival or crust incorporation efficiencies. Our integral ^{60}Fe-deposition of $(3.5\pm0.2)\times10^{7}$ ^{60}Fe atoms·cm^{-2} into deep-sea sediments for a time period between ~1.7 and 3.2 Myr can be compared to a ^{244}Pu deposition rate of <15,000 atoms·cm^{-2}·Myr^{-1} (for 0.5-2.2 Myr, 2σ-value)[6]. Similarly, the deposition into deep-sea crust samples (Crust-1, 5.9×10^{6} atoms·cm^{-2} for 0-4.35 Myr, and a flux of <188 ^{244}Pu atoms·cm^{-2}·Myr^{-1} for 0.5-5 Myr) yields a 2σ-limit of ^{244}Pu/^{60}Fe<3×10^{-5}; and for the second time period (layer 3-5 in Crust-1, 4.35-10.89 Myr) a 2σ-limit of ^{244}Pu/^{60}Fe <2×10^{-5} (~3.5×10^{6} ^{60}Fe atoms·cm^{2}, compared with the value of <66 ^{244}Pu-atoms·cm^{-2}·Myr^{-1} (5–11 Myr). Both, sediment and crust imply a ^{244}Pu/^{60}Fe atom-ratio of <10^{-4} during periods of elevated ^{60}Fe deposition over the last 10 Myr and fully agree with the recently reported low ^{244}Pu SN-yields[6].

The ISM dust grains observed with spacecrafts[15,55] follow the flow velocity of the ISM (25 km·s^{-1}) compared to the Sun's speed with respect to the Local Standard of Rest of 13 km·s^{-1}. Using as a proxy the mean of 19 km·s^{-1}, the ^{60}Fe flux becomes equivalent to a SS-concentration of 1.7×10^{-12} ^{60}Fe-atoms·cm^{-3} and represents the fraction of ^{60}Fe found in the inner SS (1.7–3.2 Myr). Furthermore, we can use our 11-Myr integrated ^{60}Fe-fluence to compare the local ^{60}Fe ISM inventory in the SS-neighborhood with the average ^{60}Fe mass distribution in the Galaxy. Our measured fluence of 2.6×10^{8} ^{60}Fe atoms·cm^{-2} within 11 Myr (~150 pc relative to Local Standard of Rest) gives an average ISM concentration of ~1×10^{-11} atoms·cm^{-3} (with 6% SS-penetration efficiency for dust). Observations of ^{60}Fe-decay in the ISM[9] and SN/AGB-models[2] suggest a production of (0.75±0.40) $M_\odot$ ^{60}Fe/Myr (equivalent to a total ^{60}Fe-mass of 2.8 $M_\odot$) in the Galaxy, whose volume is ~10^{67} cm^{3}. SN-models vary by a factor of 4 in their ^{60}Fepredictions. 2.8 $M_{\odot}$ equals 6×10^{-12} ^{60}Fe atoms·cm^{-3}. Thus, the local ^{60}Fe ISM-environment as mapped through our 11 Myr-averaged data does not significantly differ from the galaxy average.

Time resolved archives

Potential terrestrial archives need to retain time information: ice cores, sediments and deep-sea crusts and nodules are possible archives. Ice cores do not extend back beyond 1 Myr due to high accumulation rates, and hence only allow searches over that time interval (note also the excursions in the ^{14}C record at A.D. 774–775 in tree rings that points to an extraterrestrial origin[64]). Deep-sea sediments and ferromanganese crusts and nodules allow searches millions of years back in time. Indeed the study of a ferromanganese crust resulted in the first detection of extraterrestrial ^{60}Fe[10,11] in terrestrial archives after it was first discovered in iron meteorites[65]. The time resolution of deep-sea sediment cores is ~1000 times higher than for the crusts or nodules due to sedimentation rates of ~mm/kyr rather than ~mm/Myr for the crust.

For a sediment core 100% uptake efficiency is likely and a 'sharp' time signal could be more pronounced in the sediment due to its high time resolution compared to crust samples where it might be diluted for samples covering a long time period. For hydrogenetic ferromanganese crust and nodules the total ^{60}Fe influx depends also on the incorporation efficiency of iron from seawater into the crust. Further, the isotope ratio is also a function of the concentration of stable Fe in the archive. For sediment samples we preferentially prepared the authigenic phase via leaching procedures for AMS measurements.

Sample Locations

Three different time-resolved deep-sea archives were selected for the present study of extra-terrestrial ^{60}Fe. Each of these archives spans several Myr. First, sediments from a depth of ~4000m in the Indian Ocean with accumulation rates of a few mm·kyr^{-1} were chosen to provide a high-resolution record. Since these sediments are expected to accumulate 100% of the particles, and thus any ^{60}Fe attached to them, they should also provide an accurate measure of the (absolute) fluence of ^{60}Fe at Earth. Second, hydrogenous ferromanganese (FeMn) crusts were collected from the Pacific Ocean. With a growth-rate of a few mm·Myr^{-1}, i.e. a factor of 1000 slower than the sediments, these crusts strongly concentrate elements and particles present in the water column above, although the incorporation efficiency is not well-known. Finally, FeMn nodules with similar properties to the crusts were collected from the Atlantic Ocean. In total 139 individual samples from these three different archives were measured for their ^{10}Be, ^{26}Al or ^{60}Fe signatures. Each archive is described in turn below.

(1) Sections of four deep-sea sediment piston cores, extracted during the ELTANIN expeditions, were provided by the Antarctic Marine Geology Research Facility, Florida State University, US (C. Sjunneskog). The cores, E45-16, E45-21 (38°58.7'S, 103°43.1'E), E49-53 (37°51.6'S, 100°01.70'E) and E50-02, were collected from sites ~1000 km south-west of Australia in the Indian Ocean at depths of ~4200 m[35]. A preliminary chronology based on magneto-stratigraphy and radiolarian zones was already available, and yielded approximate sediment accumulation rates of 4 mm·kyr^{-1} (E45-21 and E50-02), and 3 mm·kyr^{-1} (E49-53), respectively[35]. A total of 89 samples were taken from the cores, each representing 1 cm of sediment and covering a time period of ~3 kyr. The majority of the samples was from the time interval 1.71–3.18 Myr and were on average ~30 kyr (10 cm) apart.

(2) Two large deep-sea FeMn crusts were collected in 1994 and 1999 from the equatorial Pacific Ocean, respectively: Crust-1 from a depth of 1551 m between Johnston Island and Wake Island; Crust-2 from a depth of 1342 m between Wake Island and Minami-Tori Island. With growth rates of 3-4 mm·Myr^{-1}, they cover the time interval from present to 11 Myr and 1.2–7 Myr, respectively. Their precise location is not available due to resource protection. These crusts were provided by JOGMEC (Japan Oil, Gas and Metals National Corporation).

(3) Two individual pieces of ferromanganese nodules (nodules-21 and -24) from the Atlantic Ocean were collected in 2009 during the DIVA-3 expedition on the research vessel METEOR[66] and were provided by the Senckenberg Society for Nature Research (SNG). Sample location was from the La Plata swell between the Argentine and the Brazilian basin in water depths between 4408 and 4456 m (trawl sample station Me 79-565). The sampling was performed between the co-ordinates: 035°06.54' W/26°32.30' S (start) and 035°03.00' W/026°29.52' S (end). They cover a time of ~5.4 Myr.

Sample preparation

Typically 3g of sediment was used to leach simultaneously Al, Be, Mn and Fe at HZDR. A modified version of the method of Bourlès et al.[33] and Merchel & Herpers[37] was applied and is described in Feige et al.[21] This procedure extracts the authigenic fraction of the sample containing the soluble iron phase in the ocean water. Iron oxide targets were mixed with Ag powder for AMS, Al_2O_3 with Cu and BeO with Nb powder.

Fe and Be were isolated from ~100–500 mg samples of crust material. The crust was dissolved in concentrated HCl and passed through anion and cation exchange columns. Beryllium was converted to BeO by heating in a microwave crucible and mixed with Nb powder for measurement of ^{10}Be with AMS. Fe was recovered as a hydroxide and converted to Fe_2O_3 at 350 °C in an electric furnace. The Fe_2O_3 was mixed with Ag powder for AMS.

Nodules were divided by a thin section saw into two halves. From one half, four fragments of distinct layers of each nodule were prepared for analysis by a micro chisel and a dental PROXXON drilling machine. Starting masses varied between 225 and 745 mg. Further chemical treatment was similar to that applied for the sediments.

Sample measurement - AMS method

We applied the most sensitive technique, accelerator mass spectrometry (AMS)[38,39] to detect the minute amounts of ^{60}Fe, ^{26}Al and ^{10}Be via their isotope ratios $^{60}Fe/Fe$, $^{26}Al/^{27}Al$ and $^{10}Be/^{9}Be$. The respective concentrations of the radionuclides ^{60}Fe, ^{26}Al and ^{10}Be were derived from the concentrations of the stable Fe, Al and Be determined via ICP-MS and AAS (see below).

In general, sample preparation culminated in a few mg of pure Fe_2O_3, Al_2O_3 or BeO, which was mixed with a conducting powder and pressed into sample holders for subsequent AMS. One such sample typically contained between a few 10^3 and 10^5 atoms of ^{60}Fe or ^{26}Al, and hence direct atom-counting by AMS was required. For such experiments where only a few counts are expected[40], it is crucial to suppress completely any interfering backgrounds due to stable elements of the same mass (e.g. ^{60}Ni in the case of ^{60}Fe), molecules of the same mass, and tails of the hugely more abundant stable isotopes (e.g. $^{54,56,57,58}Fe$). AMS achieves this suppression via the combination of stripping of energetic ions in the high-voltage terminal of a tandem electrostatic accelerator, magnetic and electrostatic analysis of the fast ions, and sophisticated particle detection techniques. The ^{60}Fe measurements were performed with the 14UD accelerator at the ANU[41,8] (sediments, crusts and nodules), the ^{26}Al measurements at the VERA (Vienna Environmental Research Accelerator) facility at the University of Vienna[42] (sediments) and the ^{10}Be measurements at VERA and also at the DREAMS (DREsden AMS) facility at HZDR[44] (sediments, nodules) and at MALT (Micro Analysis Laboratory, Tandem accelerator), Univ. of Tokyo[43] (crusts).

In a sputter ion source the samples were bombarded with Cs ions and negative ions extracted, and mass-analyzed before injection into the respective tandem accelerator. Following break-up of molecular ions and stripping to positive atomic ions in the high-voltage terminal of the accelerator, positive ions were accelerated to final energies between 7 and 16 MeV (^{10}Be), 12

MeV (^{26}Al) and 170 MeV (^{60}Fe) and their energies and charge states selected with a second analyzing magnet. They then had to pass additional energy and mass filters (electrostatic and magnetic separators, respectively) and were finally counted with an energy-sensitive particle detector (Supplementary Table S2).

Determination of ^{26}Al and ^{10}Be

^{26}Al measurements were performed at VERA[63] for all available Eltanin sediment samples and complemented the ^{60}Fe data. In contrast to ^{60}Fe, however, there is a terrestrial background of ^{26}Al, mainly from cosmic-ray bombardment of argon in the atmosphere, which dominates the ^{26}Al signal in the sediment samples. This allowed the possibility of ^{26}Al serving as a complementary dating tool to ^{10}Be. Any extraterrestrial ^{26}Al will sit on top of the terrestrial ‘background’. In total, 89 sediment samples were analyzed for their ^{26}Al content[21,36,54].

^{10}Be was measured at three different AMS-facilities: ^{10}Be/^{9}Be ratios of the sediment samples were determined at the VERA and DREAMS facilities. ^{10}Be in the crusts was measured at MALT. Also, at DREAMS the nodules were measured for their ^{10}Be content. The DREAMS in-house standard SMD-Be-12[44] with ^{10}Be/^{9}Be=$(1.704\pm0.030)\times10^{-12}$ was used for normalization at both facilities. About 600 μg stable ^{9}Be-carrier was added to each sample. ICP-MS and GF-AAS measurements on aliquots, taken prior to the carrier addition, gave the natural ^{9}Be concentrations. The measured ^{10}Be/^{9}Be ratios after carrier addition were between 10^{-11}-10^{-10}, well above the AMS machine background of $<10^{-15}$. From the measured ^{9}Be concentrations in the sediment samples, we deduce that the intrinsic ^{10}Be/^{9}Be ratios in the sediment are ~3 orders of magnitude higher at 10^{-8}-10^{-7}.

Stable element measurements

Measurements of stable element concentrations in aliquots (~4%) of the leachates of sediment and of the nodule samples were performed by ICP-MS (Al, Be, Ca, Fe, Mg, Mn, Ni) and GF-AAS (Be) at HZDR and at CEREGE, Aix-Marseille University, France; and by ICP-MS at MALT, for Fe, Be, Al, Mn, Co, Ni and Zn in the crust samples.

Dating of the deep-sea sediment samples

In addition to pre-existing paleomagnetic dating[35] the samples were dated using $^{10}Be/^{9}Be$ and $^{26}Al/^{27}Al$ isotope ratios. Both radioactive isotopes are produced by cosmic-ray induced spallation of atoms in the Earth atmosphere. Although ^{26}Al is produced and ejected by SN explosions, a potential SN signal of ^{26}Al may be small compared to the terrestrial background, making it useful for dating applications.

The chronology for the Eltanin cores was obtained from $^{10}Be/^{9}Be$ and $^{26}Al/^{27}Al$ data matched to the magnetic reversals as fixed tie points. Bioturbation was taken into account by assuming a mixing depth of 10 cm that corresponds to time intervals of 28 kyr and 38 kyr for E49-53 and E45-21, respectively. The ^{26}Al data suggest constant sedimentation rates for the time period analyzed here of (2.79±0.06) mm·kyr^{-1} for E49-53 and (3.73±0.18) mm·kyr^{-1} for E45-21[21,54].

^{10}Be production from cosmic rays in the Earth's atmosphere is 500 times higher than ^{26}Al production. The ICP-MS determination of ^{9}Be, however, introduced significant additional uncertainty into the intrinsic $^{10}Be/^{9}Be$ ratio that is the basis of the chronology. So, although the chronology obtained for the ^{10}Be in the ELTANIN sediment samples is in agreement with the ^{26}Al-dating for ages younger than ~3-4 Myr, the uncertainties were significantly larger.

Therefore we based our dating of the sediments also on the ^{26}Al data. At ages greater than 4 Myr, radiogenic production of ^{26}Al within the sediment might become important, leading to deviations from ages obtained from ^{10}Be dating[21,54] (publication in preparation).

Here, ages of mean values of adjacent dating points with similar ratios of $^{10}Be/^{9}Be$ and $^{26}Al/^{27}Al$ were determined using the initial ratios from surface sediment data, where $(^{10}Be/^{9}Be)_{surface}$ = $(1.08\pm0.07)\times10^{-7}$ and $(^{26}Al/^{27}Al)_{surface} = (2.56\pm0.11)\times10^{-13}$. The resulting age-depth profile matched the magnetostratigraphic tie points (time-depth positions in the deep-sea cores, where magnetic reversals occurred). By linear regression of the resulting age versus depth from both, isotopic and magnetostratigraphic data, age-profiles for E45-21 and E49-53 were obtained and applied to each sample (Supplementary Figures S10 and S11). Sediment material of E45-16 and E50-02 was dated individually applying the initial surface isotope ratios, as only a few samples were available.

Details on the determination of ^{60}Fe

We have developed the capability to detect trace amounts of ^{60}Fe in terrestrial archives by AMS with an overall efficiency (atoms detected/atoms in the sample) of up to $\sim10^{-3}$ (see Supplementary Table S2)[8]. The AMS measurements determine the atom ratio, e.g. $^{60}Fe/^{A}Fe$ where ^{A}Fe (A=54 or 56) is a stable isotope measured as an ion current in a Faraday cup in front of the particle detection system. The ANU setup has been optimized for high-measurement efficiency combined with an exceptional selectivity that is achieved owing to the high energies available from the 14UD tandem accelerator operating at ~14 MV in combination with a gas-filled magnet detection system[41,67,68]. A measurement background of $^{60}Fe/Fe=(4\pm2)\times10^{-17}$ was reached with this system (Supplementary Figure S3).

We expect $^{60}Fe/^{56}Fe$ ratios between $<10^{-16}$ and $\sim10^{-14}$ from all samples. At these ultra-low levels, the elimination of interference from the stable isobar ^{60}Ni becomes extremely challenging. Although AMS completely destroys and removes molecular ions of mass 60 in the beam with the use of the accelerator and subsequent mass filter, the stable nuclide ^{60}Ni behaves in exactly the same way through the accelerator and subsequent analyzers, and hence is still present at levels many orders of magnitudes (up to 10^{10}) above the rare ^{60}Fe. Spatial separation of the ^{60}Fe and ^{60}Ni isobars was achieved in a gas-filled magnet allowing the great majority of the ^{60}Ni to be blocked from entering the final particle detector[67,68]. A multi-electrode ionization chamber that determines not only the energy but also the rate of energy loss of each ion and its position then allows the few ^{60}Fe events to be clearly separated from the residual ^{60}Ni (Supplementary Figure S2). The gas-filled magnet reduces the ^{60}Ni intensity (typically 10^5-10^6 counts·s^{-1} despite the best efforts of the chemist) by a factor of $\sim10^4$ to a rate that the ionization detector can handle comfortably. This setup provides a powerful means to reject the ^{60}Ni isobaric background, but accepts essentially all of the ^{60}Fe events. Sputtering times were typically several hours per sample with ^{60}Fe detector count rates on average about one event per hour.

Reference samples (standards) with well-known isotope ratios were measured regularly to monitor the measurement setup. Supplementary Table S2 lists the main parameters for the AMS measurements. Due to the low number of expected ^{60}Fe (and ^{26}Al) events, the measurement background was carefully monitored with samples of iron (and aluminum) oxides that contained negligible ^{60}Fe (and ^{26}Al). These included both full chemistry blanks and unprocessed commercial material. Further, the oldest samples (>9 Myr, i.e. ~3.5 ^{60}Fe half-lives) served as additional sample blanks for ^{60}Fe because radioactive decay would have decreased this by more than an order of magnitude.

FeO^- was injected into the tandem accelerator. The system was tuned with $^{56}Fe^{11+}$ and $^{54}Fe^{10+}$ pilot beams. During measurements, the beam intensity was measured regularly as $^{54}Fe^{10+}$ current in a Faraday cup in front of the gas-filled magnet. The standard-type samples with known isotope ratios (kindly provided by D. Schumann, PSI) confirmed the validity of scaling between the different masses, with the data showing a reproducibility of ~3%.

The measurement procedure was a slow sequence of 10 s measurements of the $^{54}Fe^{10+}$ ion current, alternating with counting periods of $^{60}Fe^{11+}$ ions that were typically 20-30 min for the real samples and blanks, but were reduced to 3-5 min for the standards. All samples were measured repeatedly. The overall yield for ^{60}Fe measurements was $(0.5\text{-}1)\times10^{-3}$; i.e. one ^{60}Fe event in the detector would represent between 1000 and 2000 ^{60}Fe atoms in the analyzed sample.

References:

31. Korschinek, G. et al., A new value for the half-life of ^{10}Be by Heavy-Ion Elastic Recoil Detection and liquid scintillation counting. *Nucl. Instr. Meth. B* **268,** 187-191 (2010).

32. Chmeleff, J., von Blanckenburg, F., Kossert, K. & Jakob, D. Determination of the ^{10}Be half-life by multicollector ICP-MS and liquid scintillation counting, *Nucl. Instr. Meth. B* **268,** 192-199 (2010).

33. Bourlès, D., Raisbeck, G.M. & Yiou, F. ^{10}Be and ^{9}Be in marine sediments and their potential for dating. *Geochim. Cosmochim. Acta* **53**, 443-452 (1989).

34. Segl, M. et al. ^{10}Be-dating of a mangenese crust from the Central North Pacific and implications for ocean paleocirculation. *Nature* **309**, 540-543 (1984).

35. Allison, E. & Ledbetter M. T. Timing of bottom-water scour recorded by sedimentological parameters in the south Australian basin. *Marine Geology* **46**, 131-147 (1982).

36. Feige, J. et al. The Search for Supernova-produced Radionuclides in Terrestrial Deep-sea Archives, *Publ. Astron. Soc. Aust.***29,** 109-111 (2012).

37. Merchel, S. and Herpers, U. An Update on Radiochemical Separation Techniques for the Determination of Long-Lived Radionuclides via Accelerator Mass Spectrometry, *Radiochim. Acta* **84**, 215-219 (1999).

38. Synal, H.-A., Developments in accelerator mass spectrometry, in: K. Blaum, Y. Litvinov (eds.), 100 Years of Mass Spectrometry, *Int. J. Mass Spectrom.* **349-350**, 192-202 (2013).

39. Kutschera, W., Applications of accelerator mass spectrometry, in: K. Blaum, Y. Litvinov (eds.), 100 Years of Mass Spectrometry, *Int. J. Mass Spectrom.* **349-350**, 203-218 (2013).

40. Wallner, A. Nuclear astrophysics and AMS – Probing nucleosynthesis in the Lab, *Nucl. Instr. Meth. B* **268**, 1277-1282 (2010).

41. Fifield, L.K., Tims, S.G., Fujioka, T., Hoo, W.T. & Everett, S.E. Accelerator mass spectrometry with the 14UD accelerator at the Australian National University. *Nucl. Instr. Meth. B* **268**, 858-862 (2010).

42. Steier P. et al. Comparison of methods for the detection of ^{10}Be with AMS and a new approach based on a silicon nitride foil stack. In submission to *Journal of Mass Spectrometry* (2015).

43. Matsuzaki, H. et al. The status of the AMS system at MALT in its 20th year, *Nucl. Instr. Meth.* B **361**, 63 (2015).

44. Akhmadaliev, S., Heller, R., Hanf, D., Rugel, G. & Merchel, S. The new 6 MV AMS-facility DREAMS at Dresden. *Nucl. Instr. Meth. B* **294,** 5–10 (2013).

45. Wallner, A. et al. Precision and accuracy of ^{26}Al measurements at VERA, *Nucl. Instr. Meth.* B**172**, 382-387 (2000).

46. Bishop, S. & Egli, R. Discovery prospects for a supernova signature of biogenic origin, *Icarus* **212**, 960-962 (2011).

47. Love, S.G. & Brownlee, D. E. Heating and thermal transformation of micrometeoroids entering the earth's atmosphere. *Icarus* **89**, 26-43 (1991).

48. Trappitsch, R. & Leya, I. Cosmogenic production rates and recoil loss effects in micrometeorites and interplanetary dust particles. *Meteorit. Planet. Sci.* **48**, 195-210 (2013).

49. Knie, K. et al. Accelerator mass spectrometry measurements and model calculations of iron-60 production rates in meteorites, *Meteorit. Planet. Sci*. **34**, 729-734 (1999).

50. Peucker-Ehrenbrink, B., Accretion of extraterrestrial matter during the last 80 million years and its effect on the marine osmium isotope record. *Geochim. Cosmochim. Acta* **60**, 3187-3196 (1996).

51. Gabrielli P. et al. Meteoric smoke fallout over the Holocene epoch revealed by iridium and platinum in Greenland ice. *Nature* **432**, 1011-1014 (2004).

52. Plane, J.M.C. Cosmic dust in the earth's atmosphere. *Chem. Soc. Rev.* **41**, 6507-6518 (2012).

53. Cremonese, G., Borin, P., Martellato, E., Marzari, F. & Bruno, M. New Calibration of the micrometeoroid flux on earth. *Astrophys. J. Lett.* **749**, L40 (2012).

54. Feige, J. *Supernova-Produced Radionuclides in Deep-Sea Sediments Measured with AMS*. PhD thesis, Univ. of Vienna (2014), pp206.

55. Altobelli, N. et al. Interstellar dust flux measurements by the Galileo dust instrument between the orbits of Venus and Mars. *J. Geophys*. **110**, A07102 (2005).

56. Athanassiadou, T. & Fields, B.D. Penetration of nearby supernova dust in the inner solar system. *New Astronomy* **16**, 229-241 (2011).

57. Gall, C. et al. Rapid formation of large dust grains in the luminous supernova 2010jl, *Nature* **511**, 326-329 (2014).

58. Nozawa, T., Wakita, S., Hasegawa, Y. & Kozasa, T. Probing the physical conditions of supernova ejecta with the measured sizes of presolar Al_2O_3 grains. *Astrophys. J. Lett.* **811**, L39 (2015).

59. Gehrels, N. et al., Ozone Depletion from nearby Supernovae, *Astrophys. J.* **585,** 1169-1176 (2003).

60. Svensmark, H. Evidence of nearby supernovae affecting life on Earth. *Mon. Not. R. Astron. Soc*. **423**, 1234-1253 (2012).

61. Lugaro, M. et al. Stellar origin of the ^{182}Hf cosmochronometer and the presolar history of solar system matter (Supplement). Science **345**, 650-653 (2014).

62. Paul, M. et al. Experimental limit to interstellar ^{244}Pu abundance. *Astrophys. J. Lett*. **558**, L133–L135 (2001).

63. Wallner, C. et al. Supernova produced and anthropogenic ^{244}Pu in deep sea manganese encrustations. *N. Astron. Rev*. **48**, 145–150 (2004).

64. Miyake, F., Nagada, K., Masuda, K. & Nakamura, T. A signature of cosmic-ray increase in AD 774–775 from tree rings in Japan. *Nature* **486**, 240 (2012).

65. Goel, P.S. & Honda, M. Cosmic-Ray-Produced Iron-60 In Odessa Meteorite. *J Geophys. Res*. **70**, 747 (1965).

66. Forschungsschiff Meteor, Reise 79, 10.07.2009 – 26.10.2009, Expeditionsheft, Deep-Sea Biodiversity, Current Activity, and Seamounts in the Atlantic, Institut für Meereskunde Universität Hamburg, ISSN 0935-9974. www.ifm.zmaw.de/fileadmin/files/leitstelle/meteor/M79/M79_Expeditionsheft.pdf.

67. Paul, M. et al. Heavy ion separation with a gas-filled magnetic spectrograph, *Nucl. Instr. Meth. A* **277**, 418 (1989).

68. Knie, K. et al., *Nucl. Instrum. Methods Phys. Res., B* **172**, 717 (2000).

69. Theis, Ch., Burkert, A. & Hensler, G. *Astron. Astrophys.* **265**, 465 (1992).

Tables:

Supplementary Table S1: Summary of the three different archives.

Deep-sea archive	Cores / pieces	Location	Time period studied	Individual samples	Radionuclides measured
Sediment cores	4	Indian Ocean	0, 1.7–3.1, >4.0 Myr	52-89	^{60}Fe, ^{26}Al, ^{10}Be
FeMn crusts	2	Pacific Ocean	0 – 11 Myr	31	^{60}Fe, ^{10}Be
FeMn nodules	2	Atlantic Ocean	0 – 5.4 Myr	8	^{60}Fe, ^{10}Be

Supplementary Table S2: Summary of AMS machine parameters of the four AMS facilities used in this work.

AMS facility	Radio-nuclide	Accelerator voltage, particle energy,	Radionuclide detection	Overall efficiency	Background (at/at)
14UD – ANU[8,41]	^{60}Fe	14 MV, 170 MeV	gas-filled magnet / position sensitive ionization chamber	$\leq 10^{-3}$	4×10^{-17}
3MV – VERA[42]	^{26}Al	3 MV, 12 MeV	solid state detector	2×10^{-4}	6×10^{-16}
	^{10}Be	3 MV, 7 MeV	passive absorber & gas det.	few10^{-4}	$<10^{-15}$
6MV – HZDR[44]	^{10}Be	4.5 MV, 11 MeV	absorber foil with electro-static deflector & gas det.	$\sim10^{-4}$	$<10^{-15}$
5MV – MALT[43]	^{10}Be	4.8 MV, 16 MeV	passive absorber & gas det.	$\sim10^{-4}$	4×10^{-14}

'gas det.' means gas ionization chamber for radionuclide counting. Overall efficiency is the probability of a radionuclide (^{60}Fe, ^{26}Al, ^{10}Be) in the sample to be detected with a particle detector

Supplementary Table S3: $^{60}Fe/Fe$ isotope ratios from AMS measurement on 52 sediment samples (Eltanin) from the Indian Ocean: surface and old layers are compatible with the measurement background. Uncertainties (1σ) are pure statistical and calculated from the number of ^{60}Fe counts.

Sediment core	Sample category	No. of samples	Time period (Myr)	^{60}Fe counts detected	$^{60}Fe/Fe$ isotope ratio (10^{-15} at/at)
50-02	surface layer	2	< 0.2	1	0.05±0.05
	mid-section	1	2.23	16	1.79±0.45
	old layers	--	--	--	--
45-16	surface layer	--	--	--	--
	mid-section	3	2.65 – 2.94	27	1.75±0.34
	old layers	2	≥4	1	0.11±0.11
45-21	surface layer	3	< 0.2	1	0.05±0.05
	mid-section	15	1.78 – 2.58	129	1.61±0.15
	old layers	--	--	--	--
49-53	surface layer	--	--	--	--
	mid-section	27	1.71 – 3.18	127	1.90±0.17
	old layers	--	--	--	--
All	**surface layer**	**5**	**< 0.2**	**2**	**0.05±0.04**
	mid-section	**45**	**1.71 – 3.18**	**288**	**1.79±0.10**
	old layers	**2**	**≥4**	**1**	**0.11±0.11**
Background – commercial Fe blanks		99	--	7	0.042±0.015

doi:10.1038/nature17196

Supplementary Table S4: ^{60}Fe/Fe measurement data for the individual sediment samples (1σ)

Sample number	Age (Myr)	^{60}Fe detector events	^{60}Fe/Fe (10^{-15} at·at^{-1})	^{60}Fe/Fe (decay corr.) (10^{-15} at·at^{-1})	Fe conc. (at·g^{-1})	^{60}Fe conc. (10^{6} at·g^{-1})	Sedimentation rate (mm·kyr^{-1})	^{60}Fe dep. rate (10^{4} at/cm^{2}/kyr)
81	0	0	0.00 <0.12	0.00<0.12	6.68E+19	0.00 <0.81	2.79	0.0 <0.3
82	0	1	0.11 ±0.11	0.11±0.11	4.77E+19	0.32 ±0.32	2.79	0.1 ±0.1
83	0	0	0.00 <0.22	0.00<0.22	2.78E+19	0.00 <0.64	2.79	0.0 <0.2
85	0	1	0.13 ±0.13	0.13±0.13	4.13E+19	0.39 ±0.39	2.79	0.1 ±0.1
84	0	0	0.00 <0.16	0.00<0.16	3.00E+19	0.00 <0.52	2.79	0.0 <0.2
1	1.71	5	0.83 ±0.36	1.32±0.57	1.39E+19	1.74 ±0.75	2.79	0.6 ±0.2
2	1.75	5	2.39 ±1.13	3.82±1.81	1.57E+19	5.91 ±2.81	2.79	1.9 ±0.9
3	1.78	6	1.31 ±0.51	2.12±0.83	1.19E+19	2.45 ±0.96	2.79	0.8 ±0.3
4	1.81	5	2.01 ±0.90	3.28±1.47	1.91E+19	6.12 ±2.74	2.79	2.0 ±0.9
46	1.78	4	2.00 ±1.06	3.16±1.68	2.70E+19	8.35 ±4.50	3.73	3.6 ±1.9
47	1.81	14	2.08 ±0.56	3.32±0.89	4.86E+19	9.77 ±2.64	3.73	4.2 ±1.1
48	1.84	7	2.11 ±0.85	3.45±1.39	3.32E+19	11.26 ±4.53	3.73	4.9 ±2.0
5	1.85	0	0.00 <5.00	<8.21	1.72E+19	0.00 <14.4	2.79	0.0 <4.7
6	1.88	11	4.71 ±1.51	7.80±2.50	1.89E+19	14.60 ±4.68	2.79	4.7 ±1.5
7	1.92	11	2.56 ±0.77	4.29±1.29	1.60E+19	6.74 ±2.04	2.79	2.2 ±0.7
87	1.89	10	0.93 ±0.29	1.54±0.49	2.96E+19	4.37 ±1.39	3.73	1.9 ±0.6
50	1.91	19	2.02 ±0.46	3.37±0.77	4.07E+19	13.43 ±3.11	3.73	5.8 ±1.3
51	1.94	3	0.95 ±0.55	1.59±0.92	2.33E+19	3.55 ±2.05	3.73	1.5 ±0.9
52	1.96	23	1.24 ±0.24	2.09±0.41	3.09E+19	6.26 ±1.27	3.73	2.7 ±0.5
12	2.08	9	2.83 ±0.94	4.92±1.64	1.81E+19	8.76 ±2.93	2.79	2.8 ±0.9
13	2.11	3	0.99 ±0.57	1.73±1.00	2.63E+19	4.38 ±2.53	2.79	1.4 ±0.8
14	2.15	8	1.44 ±0.49	2.56±0.87	2.16E+19	5.38 ±1.83	2.79	1.7 ±0.6
15	2.18	1	0.33 ±10.0	0.59±17.88	1.86E+19	0.97 ±29.2	2.79	0.3 ±9.5
61	2.26	7	1.13 ±0.43	2.08±0.78	2.98E+19	5.97 ±2.26	3.73	2.6 ±1.0
62	2.29	7	2.58 ±0.92	4.77±1.71	3.65E+19	17.12 ±6.14	3.73	7.4 ±2.7
79	2.23	16	1.65 ±0.41	2.97±0.74	2.91E+19	8.42 ±2.15	3.73	3.6 ±0.9
22	2.41	3	4.62 ±2.67	8.79±5.08	6.82E+18	5.94 ±3.43	2.79	1.9 ±1.1

27	2.59	6	3.91 ±1.51	7.76±3.00	1.55E+19	11.93 ±4.86	2.79	3.9 ±1.6
68	2.47	1	1.94 ±1.94	3.75±3.75	7.50E+18	2.76 ±2.76	3.73	1.2 ±1.2
68x	2.47	1	2.19 ±2.07	4.24±4.01	7.21E+18	3.00 ±2.84	3.73	1.3 ±1.2
71	2.57	2	1.38 ±0.98	2.74±1.94	1.30E+19	3.47 ±2.46	3.73	1.5 ±1.1
63	2.32	14	1.95 ±0.49	3.62±0.92	3.45E+19	12.25 ±3.11	3.73	5.3 ±1.3
63x	2.32	6	1.80 ±0.74	3.36±1.37	3.45E+19	11.33 ±4.63	3.73	4.9 ±2.0
30	2.68	3	2.96 ±1.71	6.02±3.47	9.30E+18	5.52 ±3.19	2.79	1.8 ±1.0
31	2.71	8	4.14 ±1.46	8.71±3.08	1.64E+19	14.19 ±5.08	2.79	4.6 ±1.6
34	2.81	2	2.06 ±1.46	4.34±3.07	6.60E+18	2.81 ±1.99	2.79	0.9 ±0.6
73	2.65	11	3.00 ±0.91	6.07±1.84	2.34E+19	14.02 ±4.29	3.30	5.4 ±1.6
28	2.62	0	0.00 <3.42	< 6.86	1.64E+19	0.00 <12.0	2.79	0.0 <3.9
29	2.66	9	5.74 ±1.91	11.61±3.87	1.78E+19	20.54 ±6.89	2.79	6.6 ±2.2
35	2.85	12	2.29 ±0.66	4.86±1.40	1.53E+19	7.29 ±2.11	2.79	2.4 ±0.7
75	2.88	9	4.18 ±1.39	9.00±3.00	2.50E+19	22.30 ±7.45	3.30	8.5 ±2.9
40	3.00	3	1.15 ±0.66	2.54±1.46	1.12E+19	2.73 ±1.58	2.79	0.9 ±0.5
74	2.94	7	0.79 ±0.30	1.72±0.65	2.45E+19	4.01 ±1.53	3.30	1.5 ±0.6
38	2.95	4	3.35 ±1.68	7.32±3.66	1.56E+19	11.29 ±5.73	2.79	3.7 ±1.9
41	3.04	3	2.14 ±1.23	4.78±2.76	1.20E+19	5.62 ±3.25	2.79	1.8 ±1.1
43	3.11	5	1.16 ±0.55	2.64±1.24	9.41E+18	2.40 ±1.15	2.79	0.8 ±0.4
44	3.15	4	1.76 ±0.88	4.05±2.02	1.13E+19	4.48 ±2.24	2.79	1.4 ±0.7
45	3.18	1	0.74 ±0.74	1.70±1.70	1.19E+19	1.91 ±1.91	2.79	0.6 ±0.6
76	4-7	1	0.28 ±0.28	0.75±0.75	3.21E+19	2.07 ±2.07	2.79	0.7 ±0.7
77	4-8	0	0.00 <0.19	0.00<0.60	3.24E+19	0.00 <2.03	2.79	0.0 <0.7

Eltanin core 49-53 are samples with numbers from 1 to 45, core 45-21 with numbers 46 to 71 and 83 to 89. Eltanin core 45-14 corresponds to the numbers 72 to 77 and Eltanin 50-02 are the numbers 78 to 82.
Typical uncertainties of the Fe concentration (ICP-MS data) are 5%. The uncertainties listed reflect statistical uncertainties only.

The ages were determined from the combined $^{26}Al/^{27}Al$ and $^{10}Be/^{9}Be$ data measured in parallel for all samples[21,54] (see Suppl. Figure S11).

The deposition rates were calculated applying the measured dry density of the sediment of 1.16 g cm^{-3}.

Supplementary Table S5: $^{60}Fe/Fe$ measurement data for the individual Crust-2 samples (not background- or decay corrected data). The absolute age from ^{10}Be data is uncertain by ~0.5 Myr. Uncertainties (1σ) listed are statistical only.

Crust-2	**depth (mm)**	**^{60}Fe counts detected**	**$^{60}Fe/Fe$ isotope ratio (10^{-15} at·at^{-1})**
Layer 1	0 – 0.5	3	1.09±0.78
Layer 2	0.5– 1.0	2	1.03±0.89
Layer 3	1.0 – 1.5	16	1.24±0.38
Layer 4	1.5 – 2.0	7	1.02±0.48
Layer 5	2.0 – 2.5	14	1.73±0.57
Layer 6	2.5 – 3.0	15	0.95±0.30
Layer 7	3.0 – 3.5	8	0.79±0.35
Layer 8	3.5 – 4.0	9	0.76±0.31
Layer 9	4.0 – 4.9	14	0.54±0.18
Layer 10	4.9 – 5.8	6	0.61±0.31
Layer 11	5.8 – 6.7	1	0.10±0.13
Layer 12	6.7 – 7.7	1	0.16±0.20
Layer 13	7.7 – 8.6	0	<0.14
Layer 14	8.6 – 9.5	0	<0.11
Layer 15	9.5 – 10.4	0	<0.16
Layer 16	10.4– 11.3	0	<0.16
Layer 17	11.3 – 12.2	0	<0.32
Layer 18	12.2 – 13.2	0	<0.30
Layer 19	13.2 – 14.1	0	<0.16
Layer 20	14.1 – 15.0	1	0.09±0.11
Layer 21	15.0 – 16.0	0	<0.13
Layer 22	16.0 – 17.0	0	<0.11
Layer 23	17.0 – 18.0	0	<0.18
Layer 24	18.0 – 19.0	0	<0.48
Layer 25	19.0 – 20.0	0	<0.30
Layer 26	20.0 – 21.0	0	<0.62
background	7.7 – 21.0	1	<0.03

doi:10.1038/nature17196

Supplementary Table S6: Deposition rates and ^{60}Fe concentrations for averaged sediment data with time resolution of ~100-250 kyr (1σ).

Sediment: 100 - 200 kyr average	**Time period (Myr)**	**^{60}Fe deposition rates ($at \cdot cm^{-2} \cdot yr^{-1}$)**	**^{60}Fe concentration (10^4 $at \cdot g^{-1}$)**
surface	0 Myr	<0.1	<0.2
mid-section	1.71 – 1.85 Myr	17.1±2.9	4.7±0.8
	1.85 – 2.00 Myr	27.4±3.5	6.9±0.9
	2.00 – 2.15 Myr	16.6±3.8	5.1±1.2
	2.15 – 2.30 Myr	32.7±6.2	8.1±1.5
	2.30 – 2.60 Myr	23.9±4.3	6.0±1.1
	2.60 – 2.80 Myr	41.1±7.7	12.3±2.3
	2.80 – 2.90 Myr	26.9±5.2	7.9±1.6
	2.90 – 3.00 Myr	14.0±4.3	4.0±1.2
	3.00 – 3.18 Myr	10.2±2.6	3.2±0.8
total fluence	**1.7 – 3.18 Myr**	**35.2±4.0**	
older	~4 - 8 Myr	<2	<0.9

Supplementary Table S7: Sedimentation rates (sediments E49-53 and E45-21) and growth rates (crust, nodules).

Sediment:	**Time period (Myr)**	**sedimentation rates (mm·kyr^{-1})**	**Depth (mm)**
E49-53	1.71 – 3.18 Myr	2.79±0.06	120 – 517
E45-21	1.78 – 2.58 Myr	3.73±0.18	398 – 697
crusts:	**Time period (Myr)**	**growth rates (mm·Myr^{-1})**	**Depth (mm)**
Crust-1	0 – 10.87 Myr	2.3	0 – 25
Crust-2	1.2 – 2.05 Myr	4.7	0 – 4
nodules:	**Time period (Myr)**	**growth rates (mm·Myr^{-1})**	**Depth (mm)**
Nodule 21	0 – 1.8 Myr	1.7	0 – 3
Nodule 21	1.8 – 3.3 Myr	2.0	3 – 6
Nodule 21	3.3 – 5.4 Myr	5.2	6 – 17
Nodule 24	0 – 1.9 Myr	2.1	0 – 4
Nodule 24	1.9 – 3.3 Myr	2.9	4 – 8
Nodule 24	3.3 – 5.4 Myr	5.2	8 – 19

Supplementary Table S8: properties of various massive stars – ^{60}Fe yields and comparison with the measured ^{60}Fe influx assumed to be equally distributed within a volume of 50 pc.

Star	Initial mass $M_{init}(M_\odot)$	Stellar life time (Myr)	Ejected mass ($M_\odot$)	^{60}Fe yield (10^{-6} $M_\odot$)	$^{60}Fe/Fe|_{ejected}$ (10^{-4} g /g)	$M_{60Fe}|_{meas}$ / $M_{60Fe}|_{model}$ (%)	Reference
AGB	1.25	6500	0.69	0.3	4.1	86	Lugaro[61]
AGB	1.80	2300	1.21	0.3	2.1	96	Lugaro[61]
AGB	3	566	2.32	0.03	0.1	964	Lugaro[61]
AGB	4	254	3.21	0.5	1.5	51	Lugaro[61]
AGB	5	137	4.13	2.2	4.8	12	Lugaro[61]
AGB	6	82	5.09	3.8	6.7	7	Lugaro[61]
AGB	6.5	66	5.54	4.3	6.9	6.3	Lugaro[61]
AGB	8	37	6.97	6.4	8.2	4.2	Lugaro[61]
AGB	8.5	31	7.35	5.2	6.2	5.2	Lugaro[61]
S-AGB	7	54	6.01	3	4.5	9.0	Doherty[28]
S-AGB	7.5	44	6.44	4	5.5	6.8	Doherty[28]
S-AGB	8	37	6.87	9	11.7	3.0	Doherty[28]
S-AGB	8.5	31	7.30	14	17.1	1.9	Doherty[28]
S-AGB	9	27	7.73	14	16.2	1.9	Doherty[28]
EC-SN	8-10	27	7.7	36 – 130		0.75 – 0.21	Wanajo[27]
CC-SN	12	17	10.6	32.5	3.9	0.83	Lugaro[61]
CC-SN	15	14	13.3	90.8	6.4	0.30	Lugaro[61]
CC-SN	18	13	16.3	136	8.8	0.20	Lugaro[61]
CC-SN	25	10	23.1	114	7.2	0.24	Lugaro[61]
CC-SN	15	14	13.5	66		0.41	Rauscher[25]
CC-SN	19	12	17.1	110		0.25	Rauscher[25]
CC-SN	20	12	18	36		0.75	Rauscher[25]
CC-SN	21	11	18.9	25		1.08	Rauscher[25]
CC-SN	25	10	22.5	150		0.18	Rauscher[25]
CC-SN	13	16		11		2.5	Limongi[26]
CC-SN	15	14		58		0.5	Limongi[26]
CC-SN	20	12		41		0.7	Limongi[26]
CC-SN	25	10		25		1.1	Limongi[26]

The stellar life time was calculated as[69]

$T\,(yr) = 1.2\times10^{10}\times(M/M_\odot)^{-2.78}$ for $M < 10\,M_\odot$, and

$T\,(yr) = 1.1\times10^{8}\times(M/M_\odot)^{-0.75}$ for $M \geq 10\,M_\odot$.

The ratio $M_{60Fe}|_{meas}/M_{60Fe}|_{model}$ was calculated with $M_{60Fe}|_{meas} = 2.7\times10^{-7}\,M_\odot$, the measured ^{60}Fe-content within a volume of 50 pc diameter.

Supplementary Figures:

Supplementary Figure S1: Locations for new and previous deep-sea ^{60}Fe archives. The red circles indicate the approximate locations of the samples from archives analyzed in this work. Locations from the two previous measurements (crust 237KD, Pacific[11] and the Atlantic sediment[18]) are indicated by the stars (original world map - image credit: Credit: Reto Stöckli, NASA Earth Observatory, http://visibleearth.nasa.gov/view.php?id=73580; http://eoimages.gsfc.nasa.gov/images/imagerecords/73000/73580/world.topo.bathy.200401.3x5400x2700.jpg; modified to indicate locations of ^{60}Fe archives).

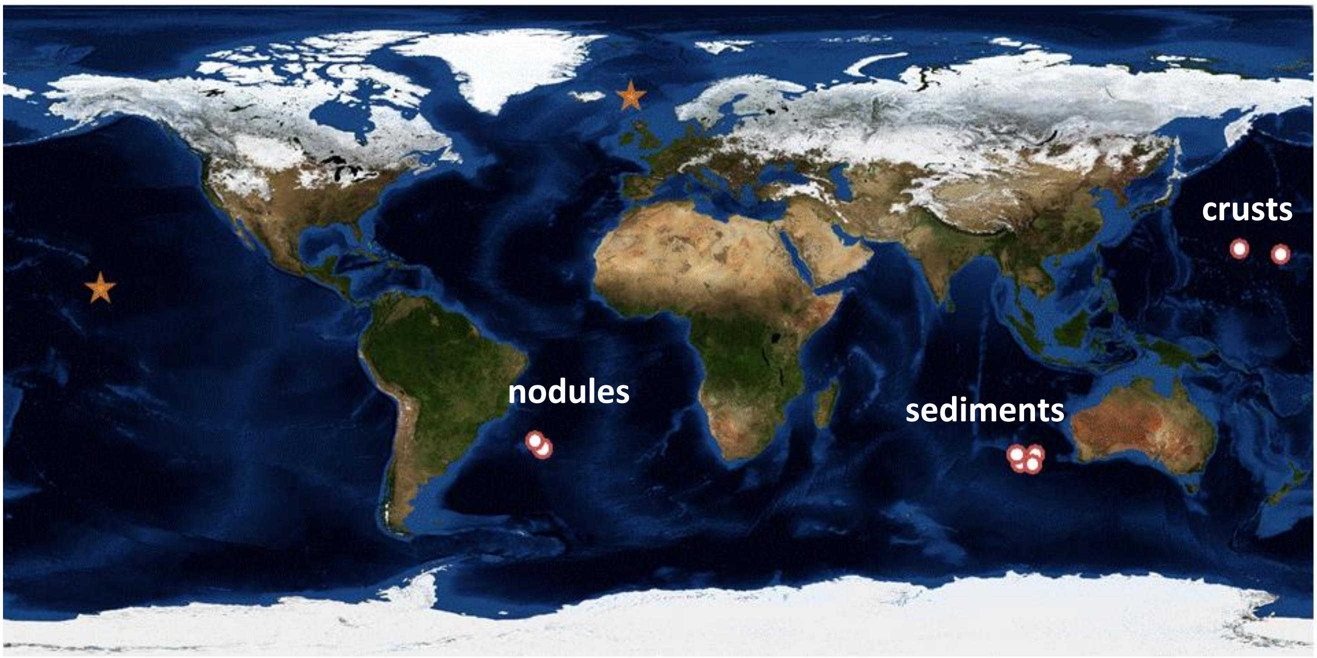

Supplementary Figure S2: Separation of ^{60}Fe from the isobar ^{60}Ni. Identification spectra with a clear separation of ^{60}Ni and ^{60}Fe obtained for a reference material with $^{60}Fe/Fe \sim 10^{-12}$. It demonstrates single atom counting of ^{60}Fe at the ANU[8]. We combined 5 different detector signals that resulted in a machine background for ^{60}Fe detection of $^{60}Fe/Fe = (4 \pm 2) \times 10^{-17}$.

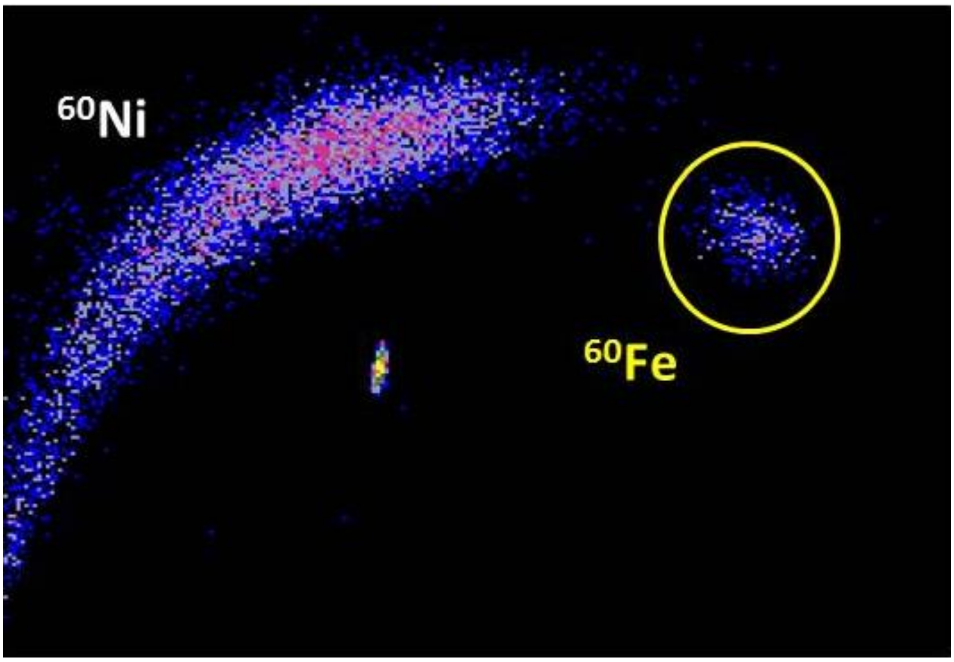

doi:10.1038/nature17196

Supplementary Figure S3: ^{60}Fe/Fe isotope ratios for sediment samples and commercial iron (Fe_2O_3) blank material. The data (1σ) for the sediment (squares) and blank material (circles, assumed to contain negligible ^{60}Fe) are plotted versus arbitrary sample numbers, i.e. without any correlation with age. The plotted blank values are the mean values for the respective measurement series (meas. series) is a factor of 43 lower than the average of the sediment samples.

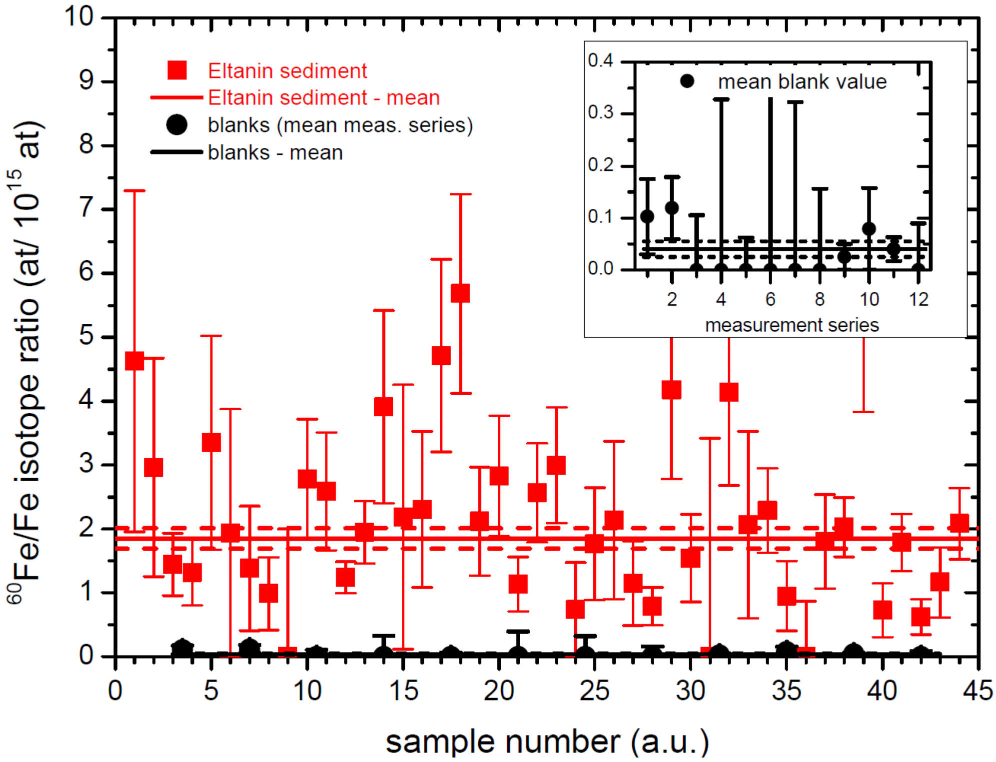

Supplementary Figure S4: Measured $^{60}Fe/Fe$ isotope ratios for the two FeMn nodule samples (no decay- or background correction, 1σ). Ages were determined from the ^{10}Be and ^{26}Al data measured in parallel. The nodule growth rates changed by more than a factor of two over the 5.4 Myr time span which leads to a systematic uncertainty in the ages of ±0.5 Myr.

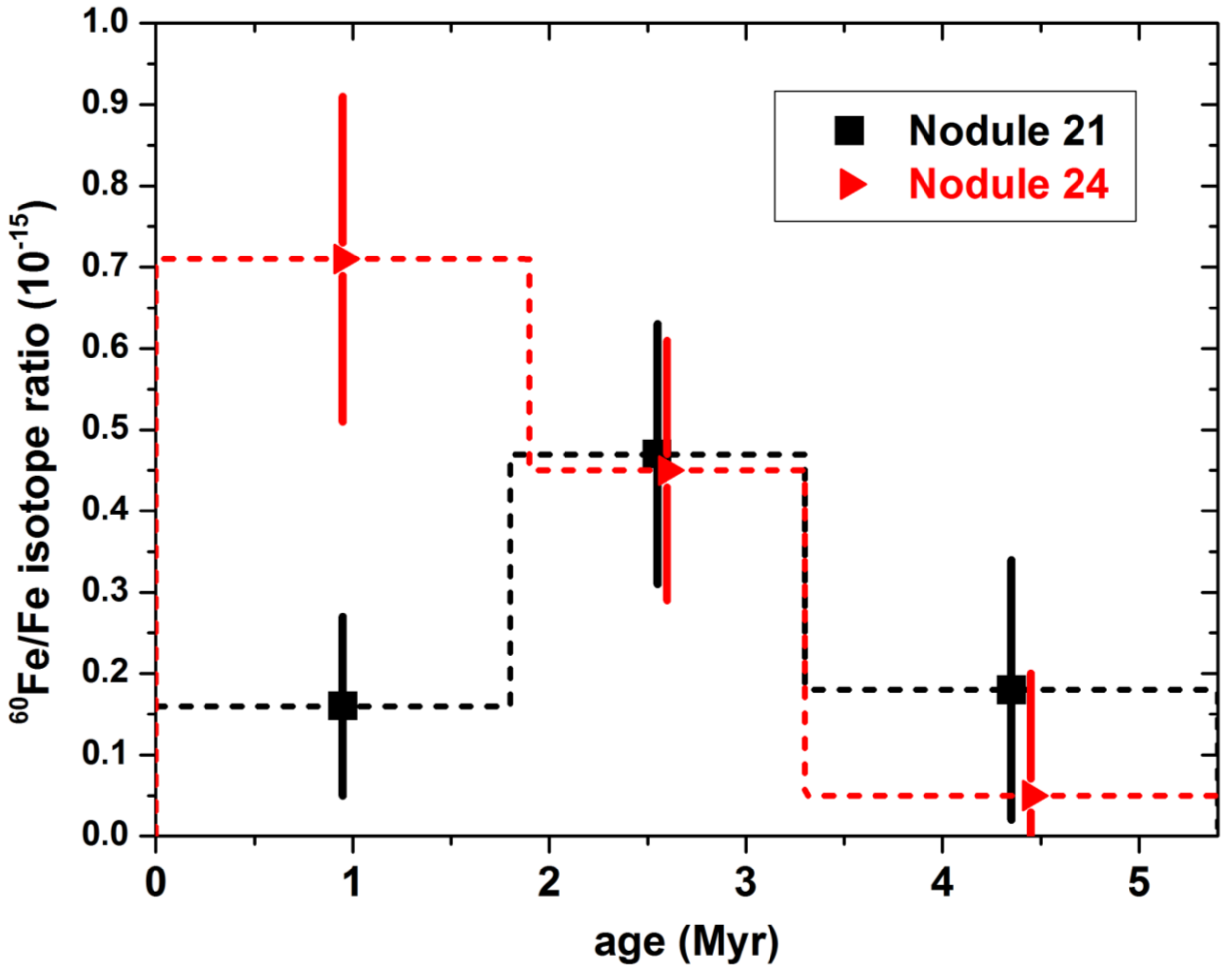

Supplementary Figure S5: 150 kyr-averages of ^{60}Fe concentrations and depositions rates for the Eltanin sediment. ^{60}Fe concentrations were on average 6.7×10^4 atoms·g^{-1} for the sediment cores between 1.7 and 3.2 Myr (1σ).

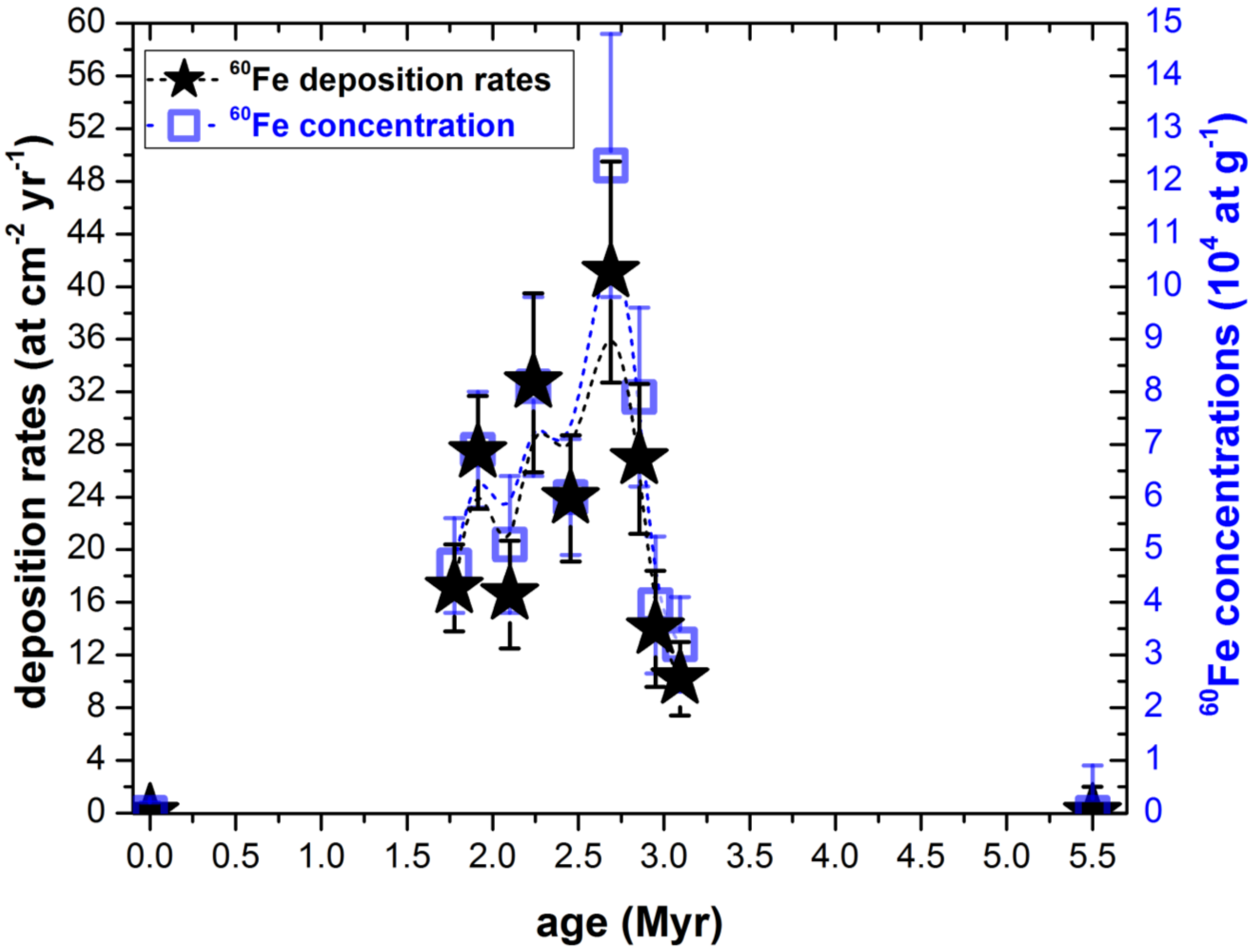

doi:10.1038/nature17196

Supplementary Figure S6: Comparison of the measured ^{60}Fe deposition rates from the sediment data (black squares) with models of interplanetary influx of ^{60}Fe. Micrometeorites (MM) and an asteroid break-up (10 km size) with a 200 kyr deposition spread are plotted. Also shown is a Gaussian-approximation of a single SN time-profile with a full-width-half-maximum of 150 kyr as a guide to the eye.

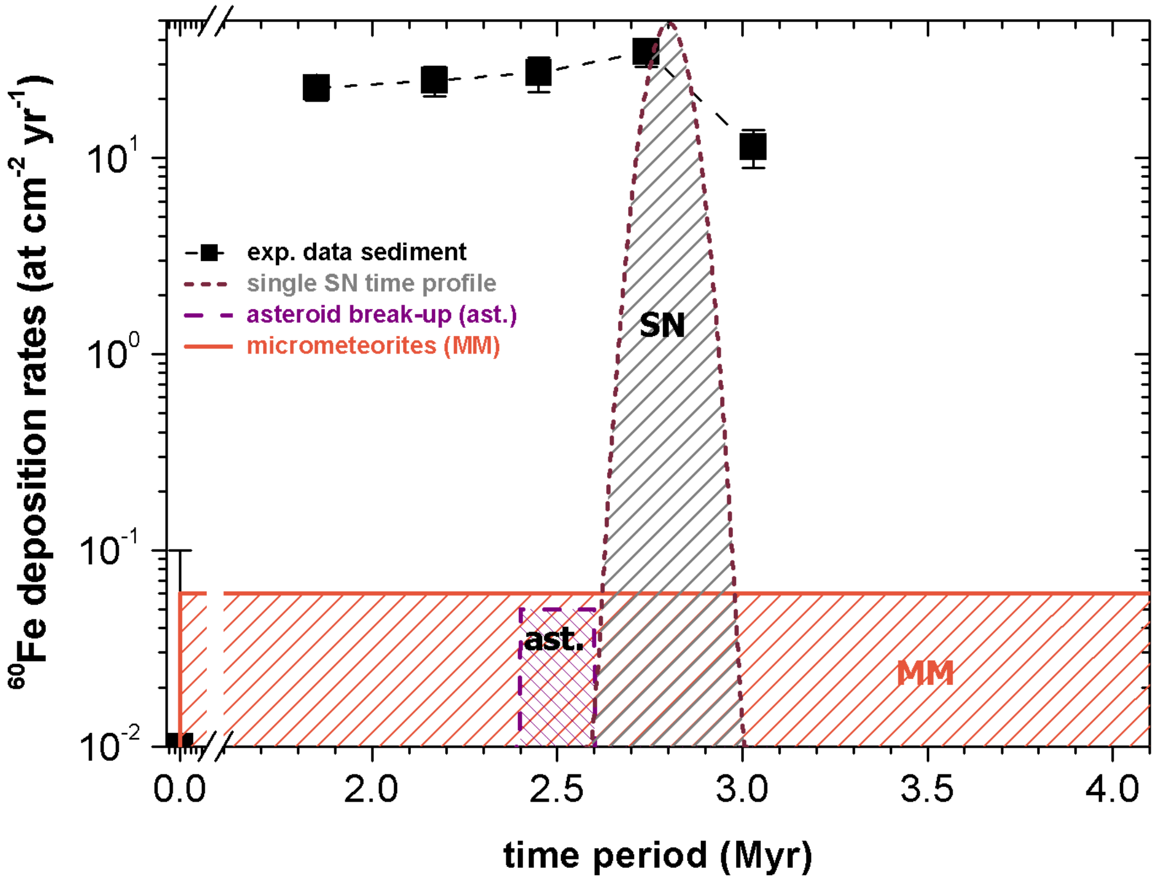

Supplementary Figure S7:

^{60}Fe survival fraction versus distance for three different ^{60}Fe SN-nucleosynthesis yields: f_{60} was calculated as the ratio of (1) ejected ^{60}Fe –assumed equally distributed over a surface area of the respective distance – and (2) the measured ^{60}Fe fluence in the inner SS $(1.5\pm0.1)\times10^8$ atoms·cm^{-2}. Note the logarithmic scale in the inset.

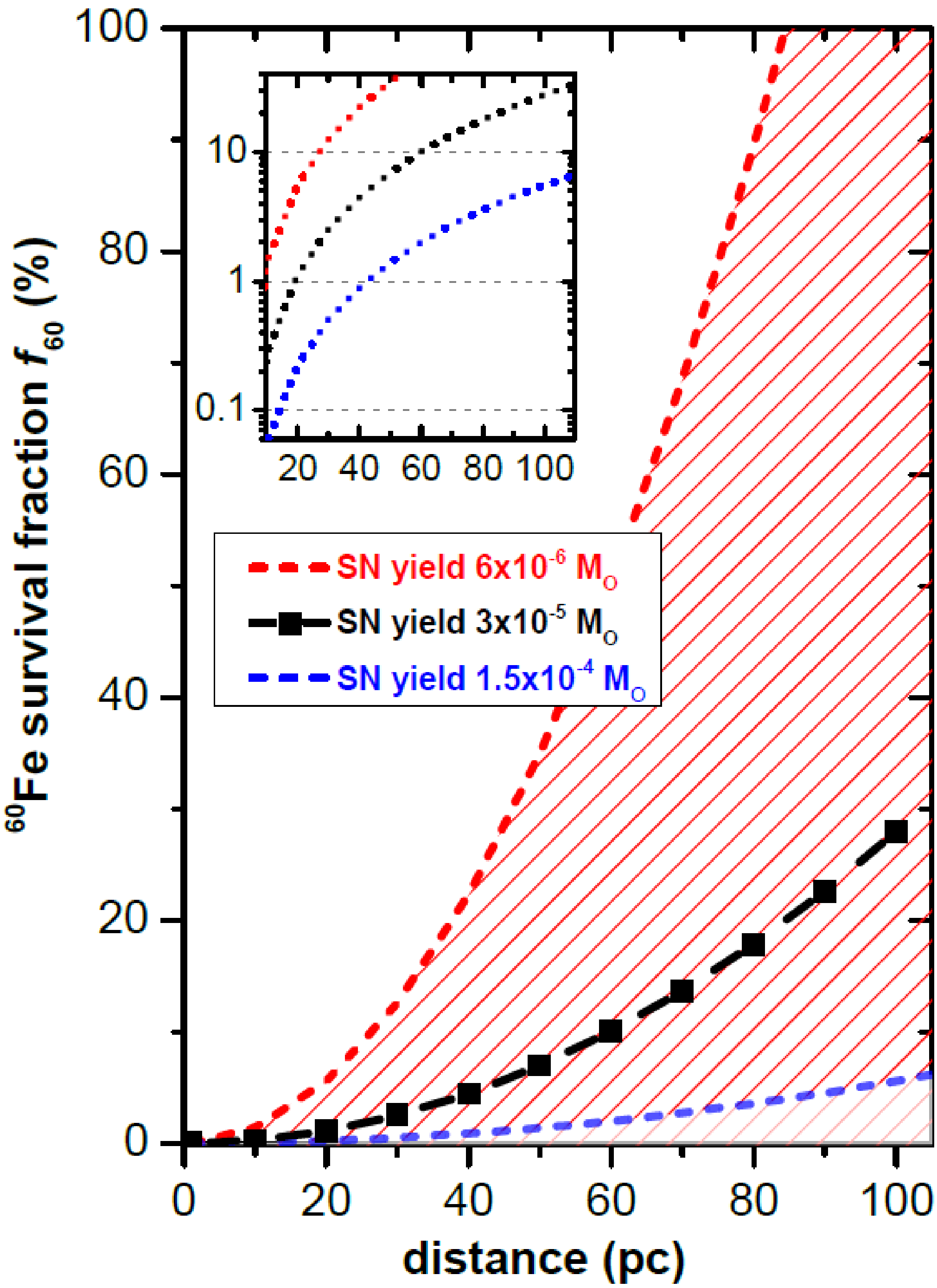

Supplementary Figure S8: ^{60}Fe nucleosynthesis yields: plotted are yields for AGB[61], SuperAGB (S-AGB)[28] as well as for SNe (EC, electron-capture[27] and CC, core-collapse[24-26,2]). For details see Supplemental Table S8. Using the measured ^{60}Fe ISM concentration (with 6% dust penetration into the SS), the band of 'experimental lower limit' indicates the mass of ^{60}Fe trapped in dust grains within a shell of size 30 pc and assuming the ejecta originate from a distance between 60 and 100 pc.

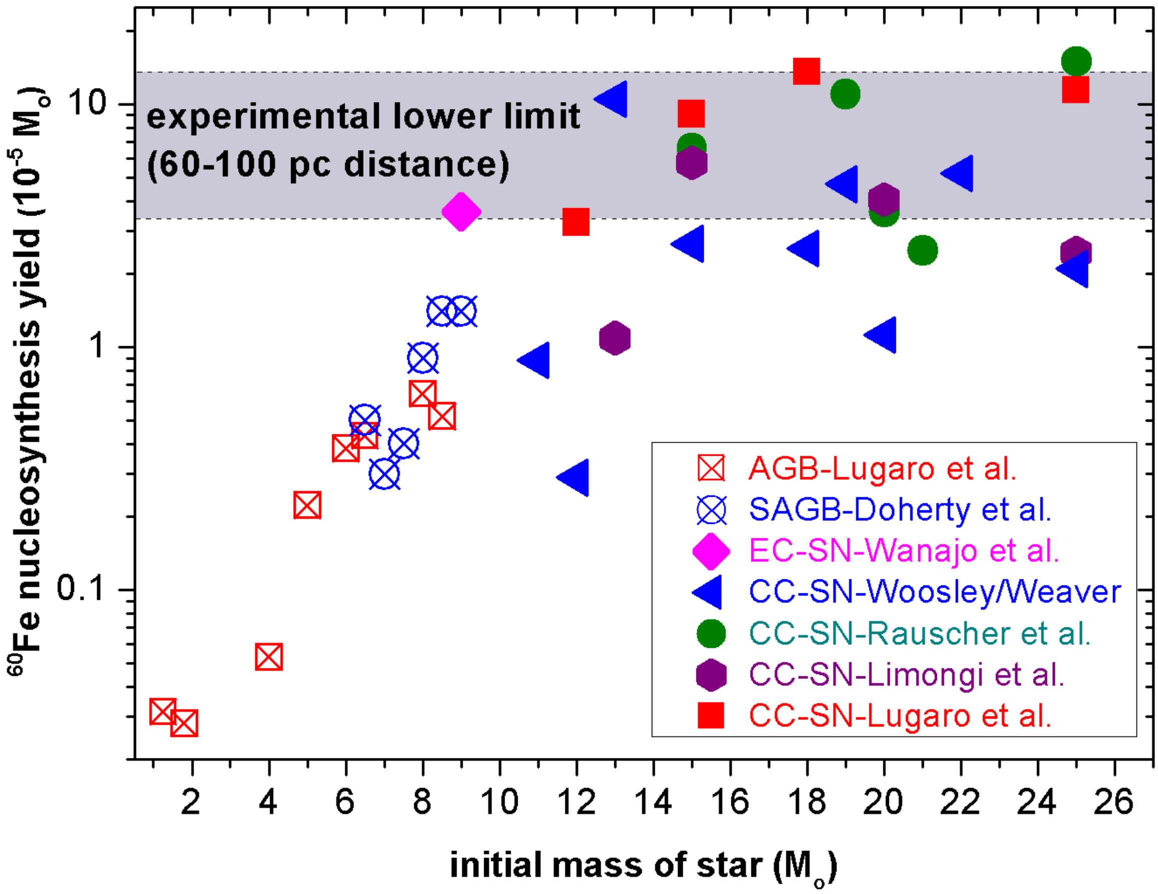

Supplementary Figure S9: measured (not decay-corrected isotope ratios) $^{60}Fe/Fe$ for the sediment samples (1σ uncertainties).

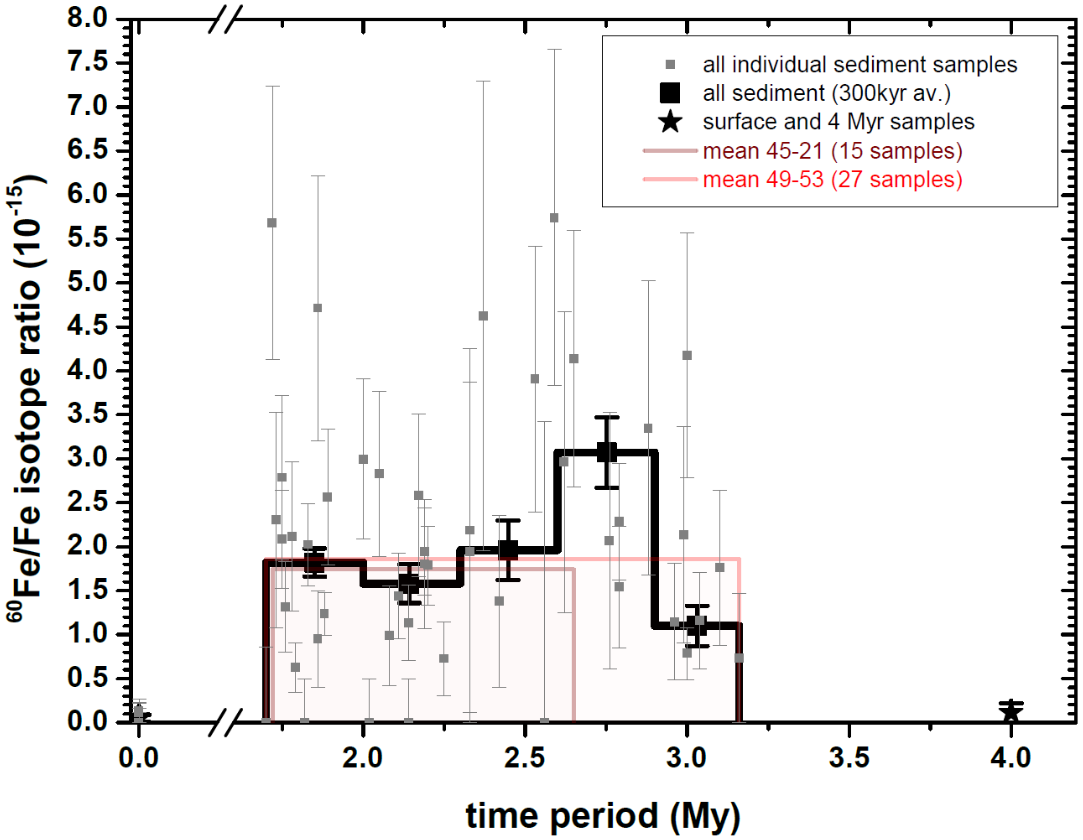

Supplementary Figure S10:

Measured (not decay-corrected) isotope ratios $^{26}Al/^{27}Al$ and $^{10}Be/^{9}Be$ isotope ratios of E45-21 and E49-53 versus age (1σ). Except for the order of magnitude, the logarithmic scale of the two ratios is similar. The solid lines indicate exponential decrease from the measured initial ratios and their uncertainties (dashed lines). Note the steeper decrease of the $^{26}Al/^{27}Al$ ratio due to the shorter half-life compared to the $^{10}Be/^{9}Be$ ratio. The scattering of individual sample ratios is within the statistic expectations; a SN signal for ^{26}Al cannot be inferred from this data. The ages fit to the previously established magnetostratigraphic dating.

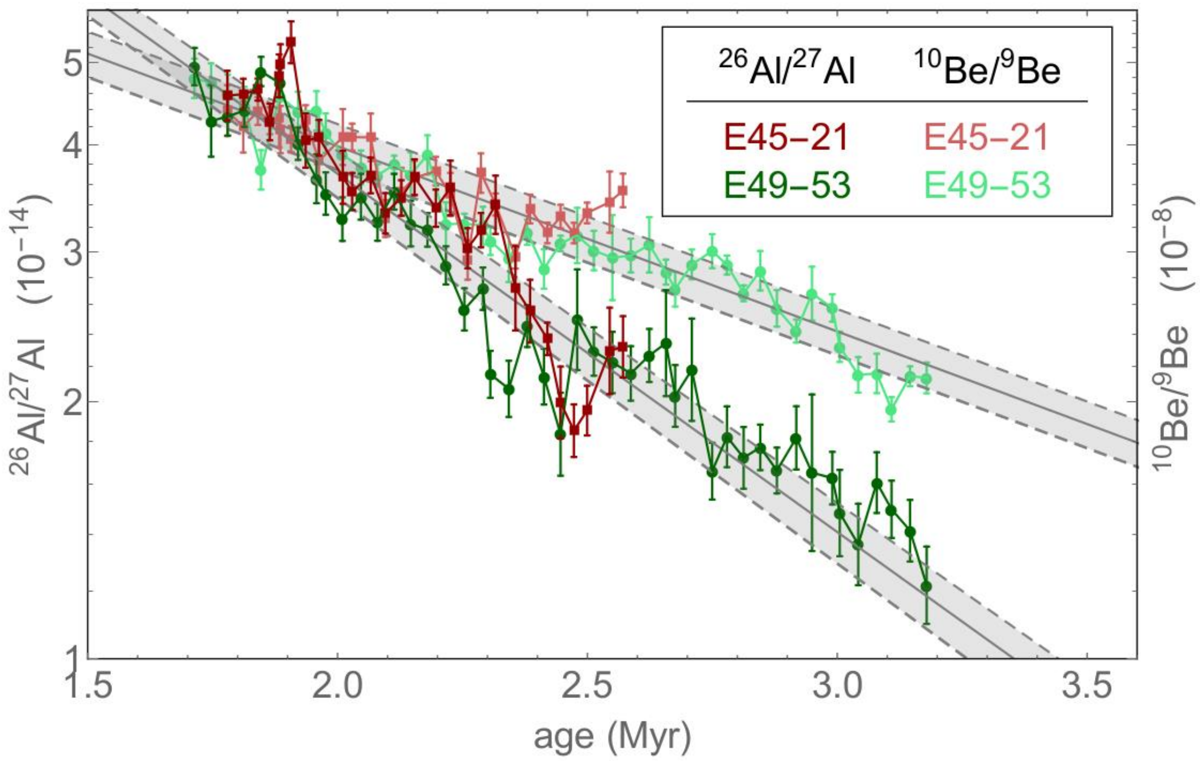

doi:10.1038/nature17196

Supplementary Figure S11:

Measured $^{10}Be/^{9}Be$ (top) and $^{26}Al/^{27}Al$ (bottom) isotope ratios for the two ELTANIN sediment cores E-49-53 and E45-21 (1σ).

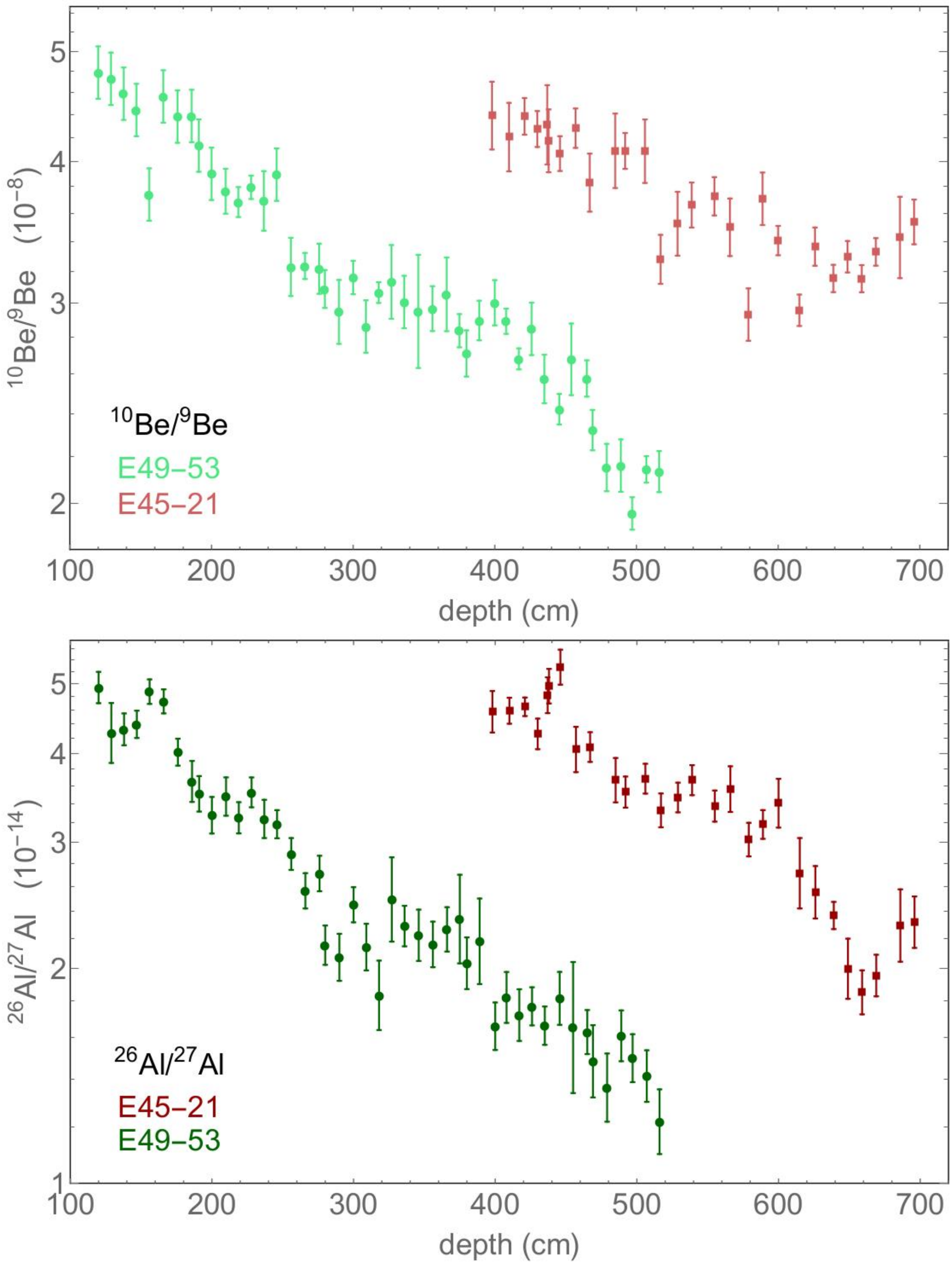

Supplementary Figure S12: **measured (not decay-corrected) $^{10}Be/^{9}Be$ isotope ratios for the two crust samples versus depth** (1σ).

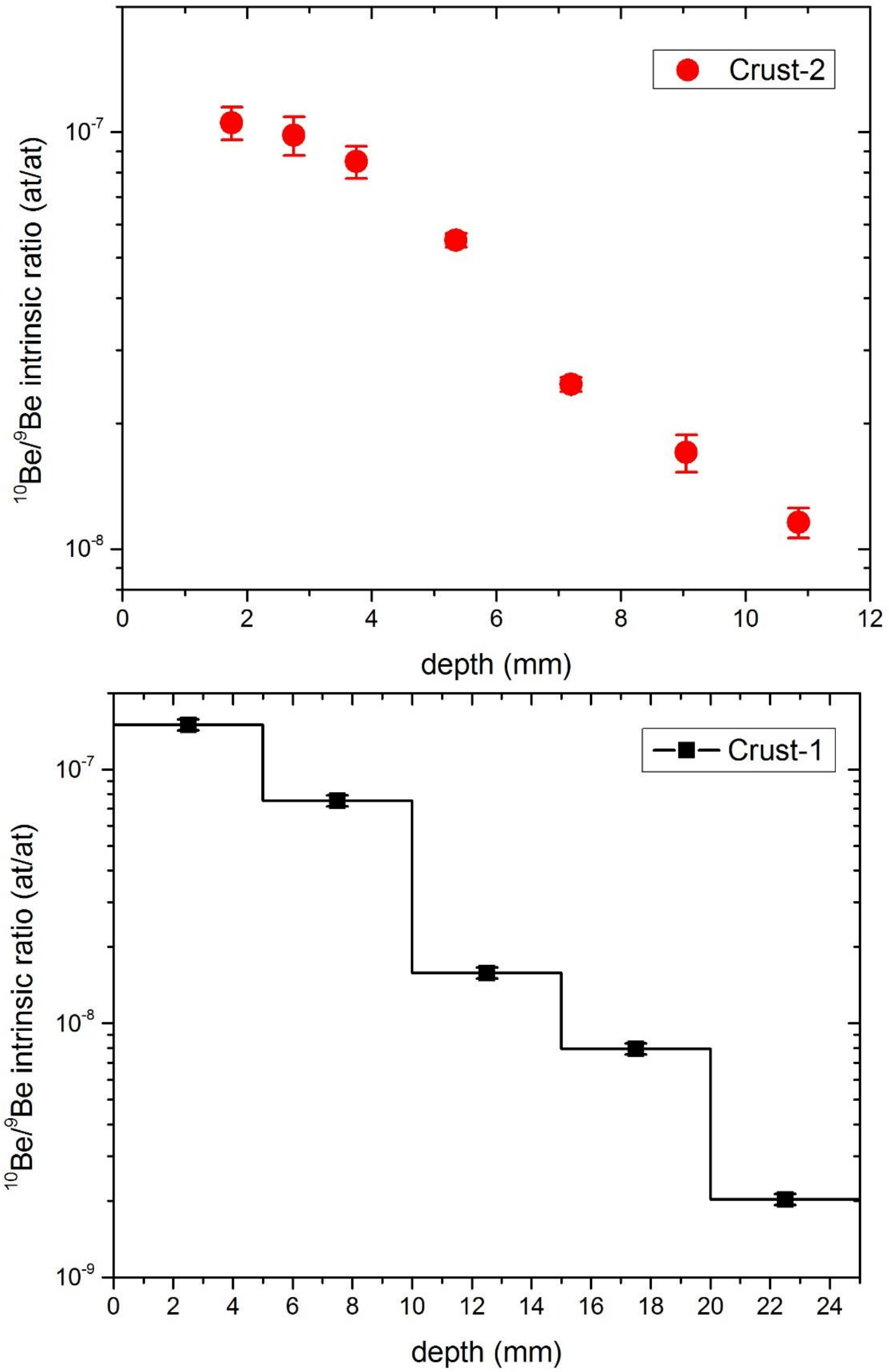

doi:10.1038/nature17196

Supplementary Figure S13: measured (not decay-corrected) $^{10}Be/^{9}Be$ isotope ratios for the two nodule samples versus depth.

The $^{10}Be/Be$ data points are plotted for depths that represent the center of the respective layers.